Geophysical Journal International

Geophys. J. Int. (2019) **00**, 1 doi: 10.1093/gji/ggz426
GJI Seismology

A physics-based approach of deep interseismic creep for viscoelastic strike-slip earthquake cycle models

Lucile Bruhat [1,2]

[1]*Department of Geophysics, Stanford University, Stanford, CA 94305, USA. E-mail:* lbruhat@stanford.edu
[2]*Now at Laboratoire de Géologie, Ecole normale supérieure, PSL Research University, CNRS UMR* 8538, 24 *rue Lhomond,* 75005 *Paris, France*

Accepted 2019 September 22. Received 2019 September 17; in original form 2019 April 23

SUMMARY

Most geodetic inversions of surface deformation rates consider the depth distribution of interseismic fault slip-rate to be time invariant. However, some numerical simulations show downdip penetration of dynamic rupture into regions with velocity-strengthening friction, with subsequent updip propagation of the locked-to-creeping transition. Recently, Bruhat and Segall developed a new method to characterize interseismic slip rates, that allows slip to penetrate up dip into the locked region. This simple model considered deep interseismic slip as a crack loaded at its downdip end, and provided analytical expressions for stress drop within the crack, slip and slip rate along the fault. This study extends this approach to strike-slip fault environments, and includes coupling of creep to viscoelastic flow in the lower crust and upper mantle. I use this model to investigate interseismic deformation rates along the Carrizo Plain section of the San Andreas fault. This study reviews possible models, elastic and viscoelastic, for fitting horizontal surface rates. Using this updated approach, I develop a physics-based solution for deep interseismic creep which accounts for possible slow vertical propagation, and investigate how it improves the fit of the horizontal deformation rates in the Carrizo Plain region. I found solutions for fitting the surface deformation rates that allow for reasonable estimates for earthquake rupture depth and coseismic displacement and improves the overall fit to the data. Best-fitting solutions present half-space relaxation time around 70 yr, and very low propagation speeds, less than a metre per year, suggesting a lack of creep propagation.

Key words: Creep and deformation; Seismic cycle; Transient deformation; Continental tectonics: strike-slip and transform; Dynamics and mechanics of faulting; Mechanics, theory, and modelling.

1 INTRODUCTION

The earliest models for interseismic deformation described a fault as a single screw dislocation in an elastic half-space, locked to some depth, but slipping at constant rate below (Savage & Burford 1970). Using this simplified model, kinematic inversions of geodetic surface rates have, for decades, been used to estimate the locking depth, presumed to delimit the depth extent of the seismogenic region.

The screw dislocation model lacks physical realism, as shown by the infinite stress concentrations at the dislocation tip. The need for more realistic models called for transitional regions between the fully locked fault and the freely creeping regions. These transitional regions involve some smoothing of the locked to creeping slip distribution, needed to mitigate the stress singularity. As a result, many inversions for interseismic slip rate include some smoothing, or simply add a linear transition from locked to creeping fault (e.g. Flück *et al.* 1997), whether or not the approach removes the stress singularity. Still, little is known about the physical characteristics of these transitional regions.

A better understanding of the mechanics of the locked-to-creeping transition is even more critical when we consider that the slip-rate distribution might not be stationary in time. While nearly all kinematic inversions of interseismic surface rates make this assumption there is no reason to believe *a priori* that this is true. Indeed, fully dynamic simulations of earthquake cycles predict that locked-to-creeping transition might evolve significantly during the earthquake cycle. Enhanced dynamic weakening behaviour in the velocity-strengthening region can allow dynamic rupture to propagate into the locked-to-creeping transition following the earthquake (Jiang & Lapusta 2016). This behaviour had already been observed in conventional rate-state models, where upward penetration of the locked-to-creeping transition occurs over lengths that scale with critical nucleation dimensions (e.g. Hetland *et al.* 2010; Hetland & Simons 2010; Segall & Bradley 2012; Jiang & Lapusta 2016).

The detection of transient slip behaviour during the interseismic cycle, such as slow slip events (Dragert 2001; Obara 2002) or decadal-scale transient events (Mavrommatis *et al.* 2014), also demonstrates that a time-invariant interseismic slip-rate distribution is not appropriate. Numerical modelling to reproduce such transient events often exhibit changes in locked-to-creeping transition during the earthquake cycle. This possibility of time-dependent slip due to shrinkage of asperities was pointed as early as Seno (2003). Simulations for slow slip events using quasi-dynamic simulations with thermal pressurization have confirmed that, between large earthquakes, the region of slow slip events gradually propagate into the locked zone (Segall & Bradley 2012). More recently, Johnson *et al.* (2016) showed that the canonical frictional model with locked asperities of fixed size was inconsistent with GPS-derived deformation in northern Japan. To address this issue, they suggested that locked asperities shrink under surrounding creep during the interseismic period (Mavrommatis *et al.* 2017). Given the presence of such time-dependent slip events, it appears difficult to support the standard definition of a fixed locked-to-creeping transition.

Bruhat & Segall (2017) recently developed a new method to characterize interseismic slip rates, that allows slip to penetrate up dip into the locked region. This simple model considers deep interseismic slip as a crack loaded at constant slip rate at the downdip end. It provides analytical expressions for stress drop within the crack, slip, and slip rate along the fault. These expressions allow the expansion of any non-singular slip rate distribution in a combination of Chebyshev polynomials. The simplicity of the method enables inversions for physical characteristics of the fault interface, establishing a first step to bridge from purely kinematic inversions to physics-based numerical simulations of earthquake cycles. When applied to observed deformation rates in northern Cascadia, best-fitting models reveal a new class of solutions, where the locking depth migrates updip with time. Best-fitting models there are consistent with a very slow updip propagation, between 30 and 120 m yr^{-1} along the fault.

In this study, I apply this model of propagating deep interseismic creep to strike-slip faults. Unlike Bruhat & Segall (2017), which considered creep propagation in a fully elastic medium, I include here the long-term deformation due to viscoelastic flow in the lower crust and upper mantle. The surface predictions greatly change when including potential viscoelastic deformation and cumulative effect of previous earthquake cycles. Purely elastic models tend to have locking depths greater than the depth of seismicity. Including viscoelastic effects (e.g. Savage & Prescott 1978; Johnson & Segall 2004) allows reasonable fits to interseismic deformation rates with shallower locking depths (e.g. Segall 2010, section 12.4.2). Obviously, physically motivated models have recently been developed (e.g. Takeuchi & Fialko 2012; Hearn & Thatcher 2015; Lambert & Barbot 2016; Allison & Dunham 2018; Zhang & Sagiya 2018) but are still rare and computationally expensive. I present here a simple method to run quickly kinematic inversions, especially in a Bayesian framework, that provides a better physical description of deep interseismic creep.

I test this new approach by investigating the interseismic deformation rates along the Carrizo Plain section of the San Andreas fault. The choice for this fault section is twofold. The model I develop is 2-D antiplane strain (infinitely long along strike), so I choose a relatively straight and simple part of a major strike-slip system. The Carrizo Plain section segment also motivated work by Jiang & Lapusta (2016) on migrating locking depth. To justify the lack of microseismicity, they suggested that the last event on this section, the M_w 7.9 Fort Tejon earthquake in 1857, could have propagated into the velocity-strengthening region beneath the nominally seismogenic zone. Even 162 yr after the last earthquake the stress concentration due to gradients in slip-rate could still be below the region where earthquakes can nucleate.

This study reviews possible models, elastic and viscoelastic, for fitting horizontal surface rates. I improve the model presented in Bruhat & Segall (2017) to account for the coupling between fault creep and viscoelastic flow. Using this updated approach, I develop a physics-based solution for deep interseismic creep that accounts for possible slow vertical propagation, and investigate how it improves the fit horizontal deformation rates for the Carrizo Plain section of the San Andreas fault.

2 METHODS

In this section, I describe the method I develop to compute interseismic deformation rates from viscoelastic earthquake cycle model including updip propagation of deep interseismic creep. Surface velocities $\mathbf{v_{horz}}$ result from (1) cumulative effect of viscoelastic earthquake cycle $\mathbf{v_{EQcycle}}$ and (2) the elastic and viscoelastic responses due to interseismic creep, respectively $\mathbf{v_{elcreep}}$ and $\mathbf{v_{vecreep}}$:

$$\mathbf{v_{horz}} = \mathbf{v_{EQcycle}} + \mathbf{v_{elcreep}} + \mathbf{v_{vecreep}} + \alpha + \epsilon \quad \text{with} \quad \epsilon \sim \mathcal{N}(0, \Sigma). \tag{1}$$

where Σ is the data covariance matrix and α a parameter that accounts for the difference in reference frames for the fault model (antisymmetric about the fault) and the measured velocities.

2.1 Viscoelastic earthquake cycle model

I first consider the contribution from repeated coseismic slip. Consider a strike-slip fault embedded in an elastic layer of thickness H, overlying a Maxwell viscoelastic half-space (Fig. 1). The fault is here considered infinitely long along strike, that is it has no along-strike variation. Every T years, an earthquake partly ruptures the fault section. To keep pace with the far-field motion, maximum coseismic displacement is $\Delta u = Tv^{\infty}$, where v^{∞} is the long-term plate rate.

Following Savage & Prescott (1978) and Segall (2010, sections 6.3 and 12.4.1), I consider the cumulative effect of K regularly spaced earthquakes at $t_{eq} = -kT$, for $k = 0, 1, ..., K$. The surface velocity v_i due to coseismic slip δ_i between z_i and z_{i+1} is then given by:

$$v_i(x, t) = \frac{\delta_i}{\pi t_R} e^{-t/t_R} \sum_{n=1}^{\infty} \frac{G_n(x, z_i, H)}{(n-1)!} \sum_{k=0}^{K} e^{-kT/t_R} \left(\frac{t + kT}{t_R} \right)^{n-1}, \tag{2}$$

where t is the time since the last earthquake. Positive is for right-lateral strike slip faults. The Maxwell relaxation time t_R of the viscoelastic medium is given by $t_R = 2\eta/\mu$, where η is viscosity and μ shear modulus. G_n are spatial operators defined by:

$$G_n(x, z_i, H) = F_n(x, z_{i+1}, H) - F_n(x, z_i, H), \tag{3a}$$

$$\text{where} \quad F_n(x, z_i, H) = \tan^{-1}\left(\frac{2nH - z_i}{x} \right) - \tan^{-1}\left(\frac{2nH + z_i}{x} \right). \tag{3b}$$

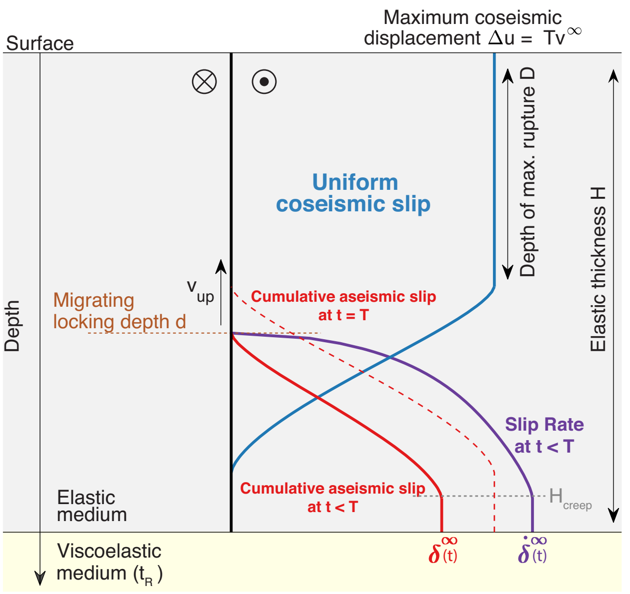

Figure 1. Model set-up for this study. The fault accommodates long-term plate rate v^∞ in a elastic medium of thickness H, which overlays a viscoelastic half-space characterized by a Maxwell relaxation time t_R. Every T years, an earthquake ruptures the upper part of the elastic crust. Maximum coseismic slip is given by Tv^∞. Coseismic rupture is uniform from the surface to depth D, then tapers. During the interseismic period, the deeper part of the fault creeps, pushing the locking depth d up at a speed $v_{\rm up}$. Interseismic slip evolves from 0 at depth d to $\delta^\infty(t)$ at depth $H_{\rm creep}$. Likewise, slip rates goes from 0 to $\dot{\delta}^\infty(t)$ at depth $H_{\rm creep}$. Slip and slip rates are constant between $H_{\rm creep}$ and the elastic thickness H. The sum of aseismic and seismic slip are set to equal plate motion at all depths.

The cumulative effect $\mathbf{v_{EQcycle}}$ of a coseismic slip distribution described by a distribution of δ_i at depth $z = z_1, .., z_i, .., z_N$ is thus

$$\mathbf{v_{EQcycle}}(x, t) = \sum_{i=1}^{N} v_i(x, t). \tag{4}$$

Expressions for corresponding stress distribution are derived in Appendix A.

2.2 Crack models for interseismic creep

Interseismic creep below the locking depth produces elastic deformation at the surface. I here review the method developed in Bruhat & Segall (2017) to describe deep interseismic creep. Consider a 1-D crack of length a, extending vertically in the elastic layer and loaded by displacement δ^∞ at the top of the viscoelastic medium (see Fig. 1). I follow the same approach of Bruhat & Segall (2017) who expanded the stress drop within the crack in Chebyshev polynomials of the first kind T_i:

$$\Delta\tau(\xi, t) = \mu \sum_{i=0}^{\infty} c_i T_i(\xi), \tag{5}$$

where c_i are the coefficients of the Chebyshev polynomials, and ξ the spatial variable such that $\xi \in [-1, 1]$. ξ is defined as $\xi = 1 - 2z/a$ such that $z \in [0, a]$ and the lower crack end $z = 0$ is fixed during crack growth. General expressions for stress drop, slip and slip rate distributions for any c_i are given in Appendix B.

For a non-singular crack driven at steady displacement, Bruhat & Segall (2017) derived values of the coefficients c_i for $i = 0, 1$. Due to the large number of unknowns already considered in the viscoelastic modelling, I will limit the number of additional parameters to invert from the crack models. In the following inversions, I restrict analysis to the simplest case where for all $i > 1$, $c_i = 0$ and $\partial c_i/\partial t = 0$. This simplification leads to the following stress drop, slip and slip rate distributions:

$$\Delta\tau(\xi, t) = \mu \frac{2}{\pi} \frac{\delta^\infty(t)}{a(t)} \xi \tag{6a}$$

$$\frac{\mathrm{d}\Delta\tau}{\mathrm{d}t}(\xi, t) = \mu \frac{2}{\pi} \frac{1}{a(t)} \left[\dot{\delta}^\infty(t)\xi + \frac{\dot{a}\delta^\infty(t)}{a(t)}(1 - 2\xi) \right] \tag{6b}$$

$$s(\xi, t) = \frac{\delta^\infty(t)}{\pi} \left[\xi\sqrt{1-\xi^2} + \arcsin(\xi) + \frac{\pi}{2} \right]. \tag{6c}$$

$$\frac{\mathrm{d}s}{\mathrm{d}t}(\xi, t) = \frac{\dot{\delta}^\infty(t)}{\pi} \left[\xi\sqrt{1-\xi^2} + \arcsin(\xi) + \frac{\pi}{2} \right] + \dot{a}\frac{2\delta^\infty(t)}{a(t)\pi}(1-\xi)\sqrt{1-\xi^2}. \tag{6d}$$

Bruhat & Segall (2017) set the bottom displacement condition to be that the crack was loaded at constant creep rate v^∞. Here I present general expressions that describe displacement and velocity conditions as $\delta^\infty(t)$ and $\dot{\delta}^\infty(t)$, which are time-dependent boundary conditions coupled to the top of the viscoelastic medium. The slip and slip-rate boundary conditions reflect the transient viscoelastic response of the mantle. Assuming that the crack started propagating after the last major earthquake, I compute $\delta^\infty(t)$ and $\dot{\delta}^\infty(t)$ to account for viscoelastic flow during this time interval. Details of the derivation of these time-dependent boundary conditions are given in Appendix C.

I use here the simplest description of the crack described in Bruhat & Segall (2017), where the stress drop distribution is linear through the crack. I could, however, increase the number of coefficients in the Chebyshev expansion to fit specific frictional properties. For instance, the creeping region could easily reproduce the slip and slip rate distributions of a region that exhibits steady velocity-strengthening. Estimates of analogous rate-state parameters, such as $a - b$, or D_c, could be inverted this way. This is out of scope for this paper, but could be used as a comparison tool for more elaborated fully numerical earthquake models.

Eq. (6d) provides an expression for slip rate along the fault. To compute elastic surface rates caused by deep interseismic creep on a fault length Λ, I combine these expressions with homogeneous half-space Green's functions G:

$$\mathbf{v_{elcreep}}(x, t) = \int_\Lambda G(x, \xi)\dot{s}(\xi, t)\mathrm{d}\xi. \tag{7}$$

I discretize the fault Λ in segments z_i and z_{i+1} for $i = 1, .., N$ such that the above expression can be approximated as discrete:

$$\mathbf{v_{elcreep}}(x, t) \sim \mathbf{G\dot{s}}. \tag{8}$$

2.3 Viscoelastic response from time-varying interseismic creep

In this section, I develop a method to compute analytically the viscoelastic response due to time-varying slip rates below the fully locked region. Consider $\dot{s}(t)$ the slip rate distribution along the fault within the region defined between the depth extent of full earthquake rupture D and the top of the viscoelastic layer H. Following Savage & Prescott (1978) and Segall (2010, section 12.4.1), the viscoelastic response associated with creep $\dot{s}_i(t)$ at depth z_i, can be written as an infinite sequence of repeating slip events at times t' extending from

$-\infty$ to current time t:

$$\hat{v}_i(x,t,z_i) = \frac{1}{\pi}\sum_{n=1}^{\infty}\frac{G_n(x,z_i,H)}{(n-1)!} \times \int_{-\infty}^{t} \dot{s}_i(t')e^{-(t-t')/t_R}\left(\frac{t-t'}{t_R}\right)^{n-1}\mathrm{d}t', \quad (9)$$

where G_n is the spatial operator defined in eq. (3a). The cumulative effect of a slip rate distribution described by a distribution of slip segments $\dot{s}_i$ between z_i and z_{i+1} for $i = 1, .., N$ is thus

$$\mathbf{v}_{\mathbf{vecreep}}(x,t) = \sum_{i=1}^{N}\hat{v}(x,t,z_i). \quad (10)$$

Now consider that the slip rate distribution $\dot{s}(t)$ can be expressed as the sum of the long-term plate motion rate and a time-dependent term. For simplicity, I assume here that prior to the most recent earthquake, that is $t < 0$, creep occurred at constant rate, and that only during the current earthquake cycle, creep is time dependent:

$$\dot{s}(t) = \begin{cases} v^{\infty} + \Delta\dot{s}(t) & \text{when } t \geq 0 \\ v^{\infty} & \text{when } t < 0. \end{cases} \quad (11)$$

The steady part v^{∞} applies to all past earthquake cycles, whereas the time-dependent term corresponds to the present cycle. Substituting this expression into eq. (9) gives:

$$\hat{v}_i(x,t) = \frac{1}{\pi}\sum_{n=1}^{\infty}\frac{G_n(x,z_i,H)}{(n-1)!}\int_{-\infty}^{t} v^{\infty}e^{-(t-t')/t_R}\left(\frac{t-t'}{t_R}\right)^{n-1}\mathrm{d}t' + \frac{1}{\pi}\sum_{n=1}^{\infty}\frac{G_n(x,z_i,H)}{(n-1)!} \times \int_{-\infty}^{t} \Delta\dot{s}(t')e^{-(t-t')/t_R}\left(\frac{t-t'}{t_R}\right)^{n-1}\mathrm{d}t' \quad (12)$$

The first term corresponds to classical solution for constant creep at speed v^{∞} from Savage & Prescott (1978). The integral can be rewritten as the Gamma function $\Gamma(n)$, which for integer values of n becomes $(n-1)!$ Eq. (12) yields

$$\hat{v}_i(x,t) = \frac{1}{\pi}\sum_{n=1}^{\infty}G_n(x,z_i,H)\left(v^{\infty} + \frac{1}{(n-1)!} \times \int_{-\infty}^{t} \Delta\dot{s}_i(t')e^{-(t-t')/t_R}\left(\frac{t-t'}{t_R}\right)^{n-1}\mathrm{d}t'\right). \quad (13)$$

Because the time-dependent term $\Delta\dot{s}(t')$ is non-zero only during the current cycle, $\Delta\dot{s}(t') = 0$ when $t' \leq 0$, leading to:

$$\hat{v}_i(x,t) = \frac{1}{\pi}\sum_{n=1}^{\infty}G_n(x,z_i,H)\left(v^{\infty} + \frac{1}{(n-1)!} \times \int_{0}^{t} \Delta\dot{s}_i(t')e^{-(t-t')/t_R}\left(\frac{t-t'}{t_R}\right)^{n-1}\mathrm{d}t'\right). \quad (14)$$

Eq. (14) gives the expression of the cumulative effect of viscoelastic flow due to time dependent creep. The first term accounts for constant creep in the region limited by z_i and z_{i+1}. The integral in the second term is calculated numerically. This model is verified against results from Johnson & Segall (2004) who computed slip and slip rate within the creeping region using a boundary element approach (details are given in Appendix D). This method reproduces adequately the results from Johnson *et al.* (2014) except when considering the very early part of the earthquake cycle. The difference originates from Johnson *et al.* (2014)'s modelling of post-seismic deformation. Their model has slip within the creeping region instantaneously after the earthquake in order to match the stress boundary condition, a condition not present in the current formulation. As a result, this method is not be appropriate for modelling afterslip at an early stage of the earthquake cycle. As I intend to study interseismic deformation that is well past the short-term post-seismic processes, I conclude that this method is adequate to reproduce viscoelastic response induced by time-dependent creep.

Fig. 2 displays slip rate profiles as a function of depth and surface velocity profiles as a function of distance due to elastic and viscoelastic response. These profiles are computed at five times during the interseismic period, and for two normalized relaxation times. Here the creeping region is modelled, following Section 2.2, by a crack lying initially between 18 and 25 km, migrating vertically at 10 m yr^{-1}. At $t = 0$ the viscoelastic response is the same as the solution for a region creeping at constant rate v^{∞}. Depending on the relaxation time, the behaviour early in the interseismic period varies. Later in the cycle, the amplitude of the viscoelastic response decreases with time and distance.

To derive eq. (14), I made the assumption that prior the most recent earthquake, creep occurred at constant rate. Now, one could think that this assumption is violated when the relaxation time t_R is really large compared to the recurrence time T, as time-dependent deformation from previous cycle should be taken into account. In fact, Fig. 2 shows that for large relaxation time t_R, the surface deformation rate due to viscoelastic flow gets closer to the solution for constant creep, than the solution for smaller relaxation time. Assuming that creep is time dependent, only during the current earthquake cycle, is not such an inadequate assumption.

3 APPLICATION TO THE CARRIZO PLAIN SEGMENT OF THE SAN ANDREAS FAULT

The previous section developed an improved description of deep interseismic creep that includes the earthquake cycle and response from viscoelastic flow. I now apply this method to investigate geodetic surface velocities across the Carrizo Plain segment of the San Andreas fault.

3.1 Deformation rates

This study considers horizontal interseismic rates in Central California provided by the SCEC Crustal Motion Model Map 4.0 published in Shen *et al.* (2011). Displacements and velocities were computed from a combination of EDM, GPS and VLBI data. Stations perpendicular to the Carrizo Plain section of the San Andreas fault are then selected (Fig. 3). I exclude stations in the Central Valley to avoid displacements perturbed by the agricultural industry. I finally project the horizontal rates onto a line perpendicular to the fault to obtain a 1-D profile of interseismic deformation.

Because this section of the San Andreas fault is too short to fully represent an infinitely long fault, I must account for 3-D effects. I use the kinematic block models developed by Johnson (2013) to compute 2-D synthetic data along a line perpendicular to the Carrizo Plain section of the San Andreas fault. This model considers the entire extent of the San Andreas fault in Central and Southern California. For this correction only, I assume the San Andreas fault locked to 19 km depth (Smith-Konter *et al.* 2011) and fully creeping in the northern creeping section. From the surface velocities due to an infinitely long fault also locked to 19 km, I compute the difference between the 1-D and the 2-D models; these are considered as a

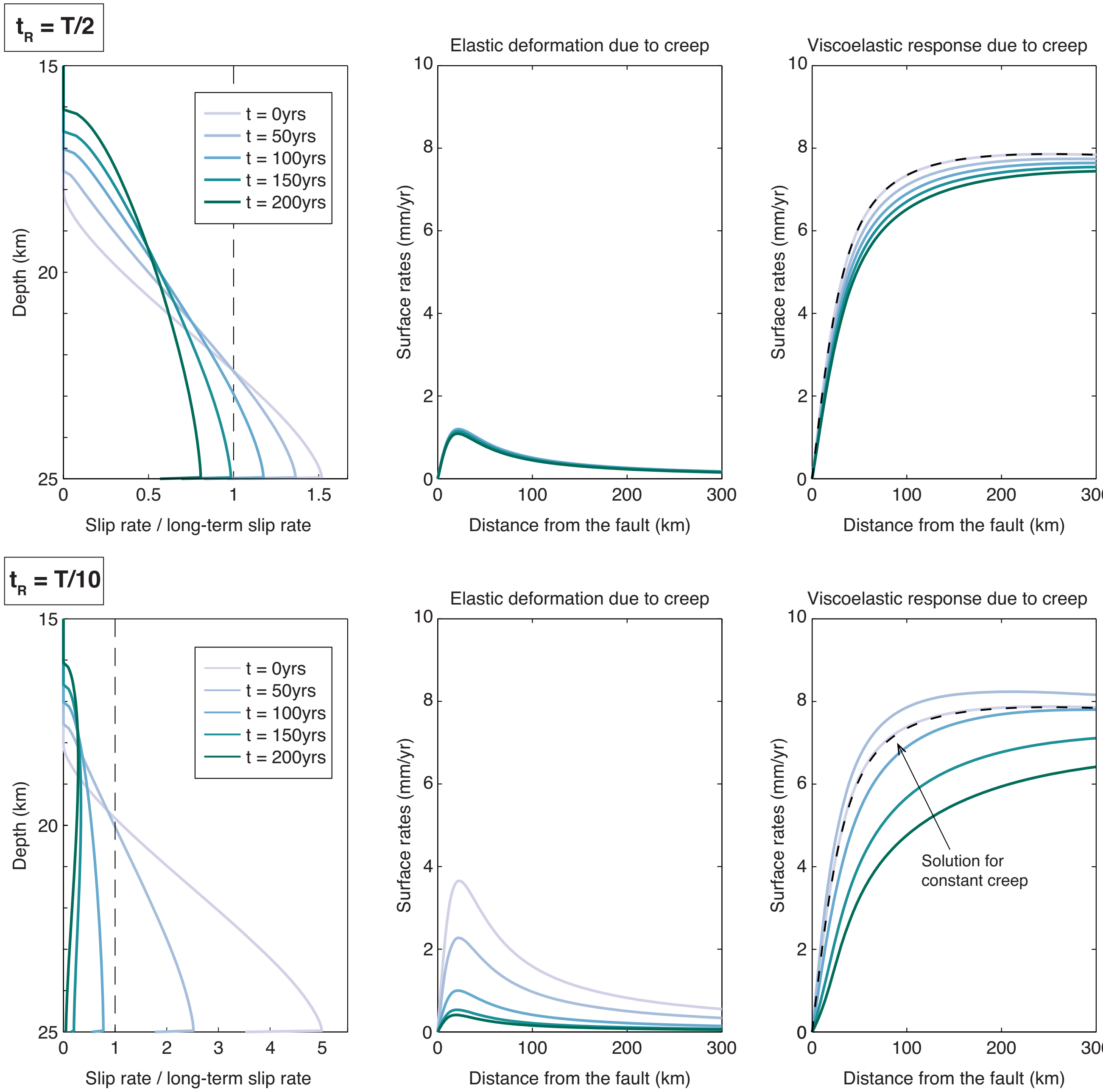

Figure 2. Elastic and viscoelastic deformation induced by time-varying creep when $t_R = T/2$ and $t_R = T/10$. The creeping region is described by a crack lying initially between 18 and 25 km, migrating vertically at 10 m yr^{-1}. Left-hand panels show the slip rate profiles in the region between the rupture region and the top of the viscoelastic layer. Middle panels show the elastic surface rates caused by interseismic creep. Right-hand panels give the viscoelastic surface rates using eq. (14). Dashed back line is the solution for a region creeping at constant rate v^{∞}.

correction for 3-D effects, as described in detail in Appendix E. This leads to a correction of approximately 1 mm yr^{-1}, and not symmetric across the fault trace (see Fig. E1).

Finally, I correct the data set for the effect of the right-lateral Hosgri fault. This fault system located at the southwestern extent of the considered section presents measured current interseismic deformation. As distant deformation rates strongly affect the fit in a viscoelastic inversion, I correct for the effect of the Hosgri fault. I use results from Johnson & Watt (2012) & Johnson *et al.* (2014) that indicate a lateral slip rate of 2.6 ± 0.9 mm yr^{-1}, considered as a minimum rate for the Hosgri fault given the presence of an active western strand. I take a locking depth of 12 km from Hardebeck (2010) used in UCERF 3 modelling [see Appendix A from UCERF 3 report (Field *et al.* 2014)]. The corrected data are displayed in Fig. 3.

3.2 Current knowledge of fault coupling and earthquake characteristics

Paleoseismic studies provide constraints on the surface coseismic slip. Although earliest measurements suggested surface displacements up to 10 m along the Carrizo Plain segment (Sieh 1978), these estimates have been reevaluated since to lower estimates, around 5–7 m (Zielke *et al.* 2010; Scharer *et al.* 2014). In this study, I impose

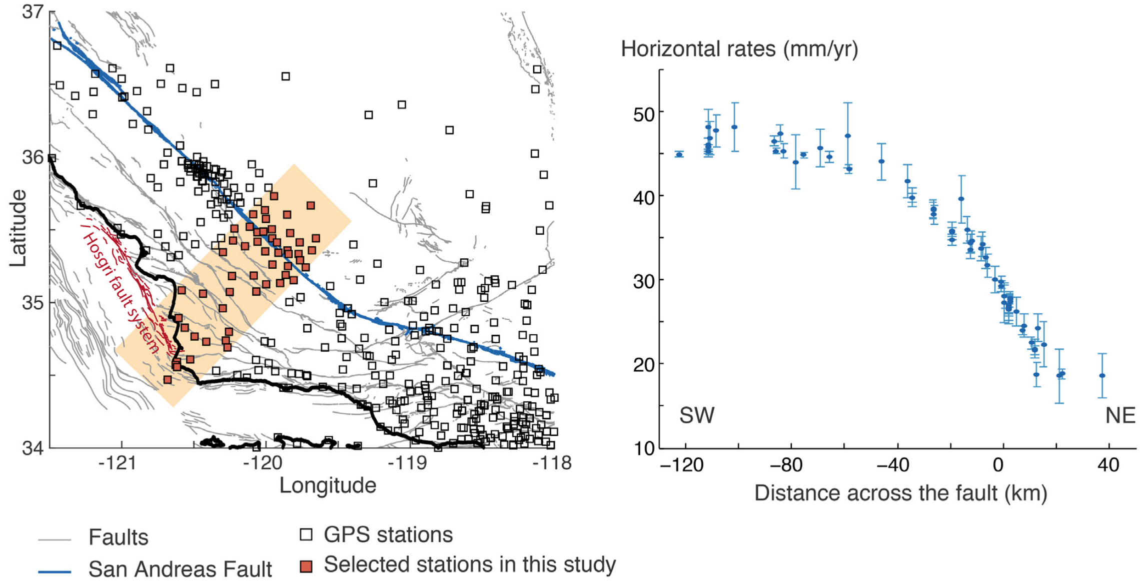

Figure 3. Data set used in this study. Left-hand panel: map of central and southern California fault system with selected stations. The San Andreas fault is denoted in blue. Right-hand panel: fault parallel component of interseismic velocities relative to the North American Plate for the selected stations. The presented rates are corrected for 3-D effects and the Hosgri fault.

the coseismic slip distribution (Fig. 1). For simplicity, I will consider that the coseismic displacement is constant with depth down to the full rupture depth D recognizing that in fact it must be tapered. A reasonable estimate for the maximum coseismic displacement in this study will be 8 m.

Classical dislocation models define the locking depth as the greatest depth of slip deficit. In this study, the locking depth is defined as the upper (shallowest) limit of the interseismic slip rate (Fig. 1). Since I assume that the sum of aseismic and coseismic slip are set to equal plate motion at all depths, the upper (shallowest) bound of the locking depth is given by the extent of the maximum coseismic displacement. Across the Carrizo segment of the San Andreas fault, numerous studies have estimated over the past decades the locking depth, using different modelling approach from elastic dislocations to fully numerical models. In 2010, a Southern California Earthquake Center (SCEC) workshop compiled these estimates through an exercise where participants were asked to fit the geodetic surface rates using whatever method they preferred (see https://www.scec.org/workshops/2010/gps-ucerf3/index.html). The mean locking depth estimated from nine independent analyses of the same geodetic data set was then 16.7 ± 2.2 km. Likewise, using a geodetically constrained semi-analytic dislocation model for the entire Southern California fault system, Smith-Konter *et al.* (2011) found locking depths around 18.7 ± 2.0 km across the Carrizo Plain segment. In this study, I consider that a reasonable estimate on the locking depth around or less than 16.7 km.

Geological studies, such as Noriega *et al.* (2006), provide bounds on long-term plate motion rate v^{∞} around 30–37 mm yr^{-1} at the Carrizo Plain segment. More recently, using a suite of inversions with four kinematic models, some of them including viscoelastic flow, Johnson (2013) found that slip rates range from 29 to 37 mm yr^{-1} for the Carrizo segment of the San Andreas Fault. In this study, I bound v^{∞} to 29–37 mm yr^{-1}.

Records of microseismicity also provide information on fault coupling. Using the earthquake catalog from Lin *et al.* (2007), Smith-Konter *et al.* (2011) examine seismicity profiles along the San Andreas fault to define the thickness of the seismogenic layer. Across the Carrizo Plain segment, microseismicity is first estimated to extend down to at 14–16 km. Using the SCSN relocated earthquake catalog for Southern California, downloaded from http://scedc.caltech.edu/research-tools/alt-2011-dd-hauksson-yang-shearer.html (Lin *et al.* 2007; Hauksson *et al.* 2012), most of the seismicity is located at depths 8–12 km, but extends to as much as 18 km. This helps constrain reasonable upper bounds on the elastic thickness H and the current locking depth.

3.3 Slip rate inversions

In this section, I describe the inversions that will be carried out in the next section. Surface velocities $\mathbf{v_{horz}}$ results from the cumulative effect of viscoelastic earthquake cycle $\mathbf{v_{EQcycle}}$, and the elastic and viscoelastic responses due to interseismic creep, respectively $\mathbf{v_{elcreep}}$ and $\mathbf{v_{vecreep}}$:

$$\begin{aligned}\mathbf{v_{horz}} &= \mathbf{f}(H, D, t_R, \Delta u, v_\infty, d, v_{up}, H_{creep}, \alpha),\\ &= \mathbf{v_{EQcycle}} + \mathbf{v_{elcreep}} + \mathbf{v_{vecreep}} + \alpha + \epsilon \quad \text{with} \quad \epsilon \sim \mathcal{N}(0, \Sigma),\end{aligned} \tag{15}$$

where Σ is the data covariance matrix and α a parameter that accounts for reference frame offset. Equations for $\mathbf{v_{EQcycle}}$ are given in Section 2.1. $\mathbf{v_{elcreep}}$ relates to the unknown vector of slip-rates $\dot{\mathbf{s}}$ via elastic homogeneous half-space Green's functions $\mathbf{G}$. Equations for the viscoelastic response $\mathbf{v_{vecreep}}$ are given in Section 2.3 using expressions for interseismic slip rates given in Section 2.2. Inversions search for the elastic thickness H, the rupture depth D, the present-day position of the locking depth, defined by the top of the creeping region d, the long-term plate motion rate v^{∞}, the viscoelastic relaxation time $t_{\rm R}$, and the maximum coseismic displacement Δu, related to the earthquake recurrence time T. To account for the possibility of a region of constant creep at the transition between the elastic and the viscoelastic region, I invert for the bottom depth of the creeping region $H_{\rm creep}$ (see Fig. 1). Between $H_{\rm creep}$ and H, the fault slips at the constant speed $\dot{\delta}^{\infty}$ defined in Section 2.2.

Table 1. *A priori* bounds for MCMC inversions.

Parameter	Symbol	Minimum	Maximum
Maximum depth of full earthquake rupture (km)	D	5	10
Long-term fault slip rate (mm yr^{-1})	v^{∞}	29	37
Elastic thickness (km)	H	18	100
Half-space relaxation time (yr)	t_{R}	0	500
Coseismic displacement (m)	Δu	4	8
Present-day locking depth (km)	d	D	H
Depth of constant creep (km)	H_{creep}	d	H
Recurrence time (m yr^{-1})	T	$\Delta u/v^{\infty}$	$\Delta u/v^{\infty}$
Propagation speed (m yr^{-1})	v_{up}	$(d\text{-}D)/(T\text{-}162)$	$(d\text{-}D)/(T\text{-}162)$
Time since 1857 earthquake (yr)	t	162	162 (fixed)
Block motion (mm yr^{-1})	α	None	None

Finally, in order to be consistent with microseismicity data, I will consider solutions whose peak in stress rate lies in the same region as the current seismicity (between 8 and 13 km). This is an important point in this inversion. This updated model allow us to derive the distribution of shear stress rate within the creeping region. While this inversion is directed by horizontal geodetic rates, I assume that the highest rate should coincide with the location of maximum shear stressing rate, which is indicated by the region of largest moment release from the microseismicity.

The coseismic slip distribution is defined as followed. From the surface to the full rupture depth D, the coseismic slip distribution is equal to the maximum coseismic displacement Δu. To ensure that at the end of the cycle, slip along the entire fault is equal to the maximum coseismic displacement, the coseismic slip distribution between D and H_{creep} is defined as the complement of the aseismic slip distribution at the end of the cycle (see Fig. 1). In other words, I not only integrate up to the current time, but also to the end of the cycle, $T = \Delta u/v^{\infty}$. Likewise, I bound the migration speed v_{up} such that slip in the elastic region is equal to Δu at the end of the cycle. The creeping region must reach the downdip limit of the coseismic region at the end of the earthquake cycle:

$$v_{up} = \frac{d - D}{T - 162}. \tag{16}$$

This study aims at developing inverse methods to test different models of interseismic deformation, accounting in some cases for propagating deep creep. Since I consider viscoelastic deformation I estimate at least the rupture depth D, the elastic thickness H, the viscoelastic relaxation time t_{R}, the coseismic displacement Δu, the long-term plate motion rate v^{∞} and α. When considering models with propagating deep interseismic slip, I also invert for the locking depth d, and deduce the propagation speed v_{up}. I use Markov Chain Monte Carlo (MCMC) methods for the inversions. MCMC algorithms efficiently estimate the maximum-likelihood solution and enable the construction of posterior distributions. I assume that the loading time t that appears in eq. (6) is fixed at 162 yr, since the last earthquake occurred in 1857. Depending the inversions, prior knowledge about the other model parameters will be included. *A priori* bounds are summarized in Table 1.

4 RESULTS

In this section, I present the results of this inversions to fit geodetic rates across the Carrizo Plain section of the San Andreas. I first found best-fitting solutions for classical inversions that consider either the fault to be a single dislocation in a fully elastic medium, or models that include a region of steady creep above a viscoelastic region. I also consider solutions from the boundary element method developed by Johnson & Segall (2004). I finally apply the method I developed including propagating deep interseismic creep. Different creep models are sketched in Fig. 4.

Inversions details are summarized in Table 2, and best-fitting parameters and confidence intervals are given in Table 3. Recall that due to the skewness of some posterior distributions, the best-fitting solution might not lies within the 95 per cent confidence interval. The results of the inversions are summarized in Fig. 5. The posterior distributions of the full rupture depth D, the elastic thickness H, the coseismic displacement Δu, the relaxation time t_{R}, the recurrence time T, the locking depth d, and propagation speed v_{up} are displayed for the four inversions. Best fits and log-likelihood distributions are shown in Fig. 6.

I first perform classical inversions to explain the deformation rates across the Carrizo Plain segment. Best-fitting parameters will provide insights on expected fault parameters inferred from this set of data, before launching more complicated inversions. I first consider a single dislocation within an elastic medium ($d = D$). Because I only invert for the maximum depth of uniform coseismic slip and long-term velocity in this model, resulting distribution are only shown for the depth D. The inverted locking depth is 10 km and long-term plate rate v^{∞} 30.1 mm yr^{-1}.

The remaining inversions consider the fault to be embedded in an elastic layer lying over a viscoelastic medium. Inverted parameters are the coseismic uniform depth D, elastic thickness H, relaxation time t_{R}, coseismic displacement Δu and v^{∞}. The first inversion considers creep at constant velocity v^{∞} between D and H (as in Savage & Prescott 1978). Best-fitting solutions indicate rupture depth of 10 km and elastic thickness of 18 km. Maximum coseismic displacement reaches 8 m. This model favours a short relaxation time, of around 39.2–55 yr. Recurrence time T ranges from 216.8 to 226.5 yr. The second inversion assumes the creeping region to slip at constant resistive stress. This is the model developed by Johnson & Segall (2004). Best-fitting parameters also reaches 10 km for D and 8 m for Δu. Unlike the previous inversion, this model infers slightly higher values for the elastic thickness H, between 17.6 and 19.4 km, and shorter recurrence time, around 215 yr. The estimated relaxation time t_{R} is two to three times higher than the one in the previous inversion.

Finally, I perform the inversion using my model. Uniform rupture depth is estimated between 9.1 and 10.3 km. Estimates of elastic thickness vary from 17.1 to 21.5 km. Coseismic slip is in the range 6.9–8.3 m. Recurrence time lies between 209 and 221 yr. Current locking depth lies between 9.2 and 10.5 km, colocated at the location of most of the microseismicity. Finally, rates for propagating creep

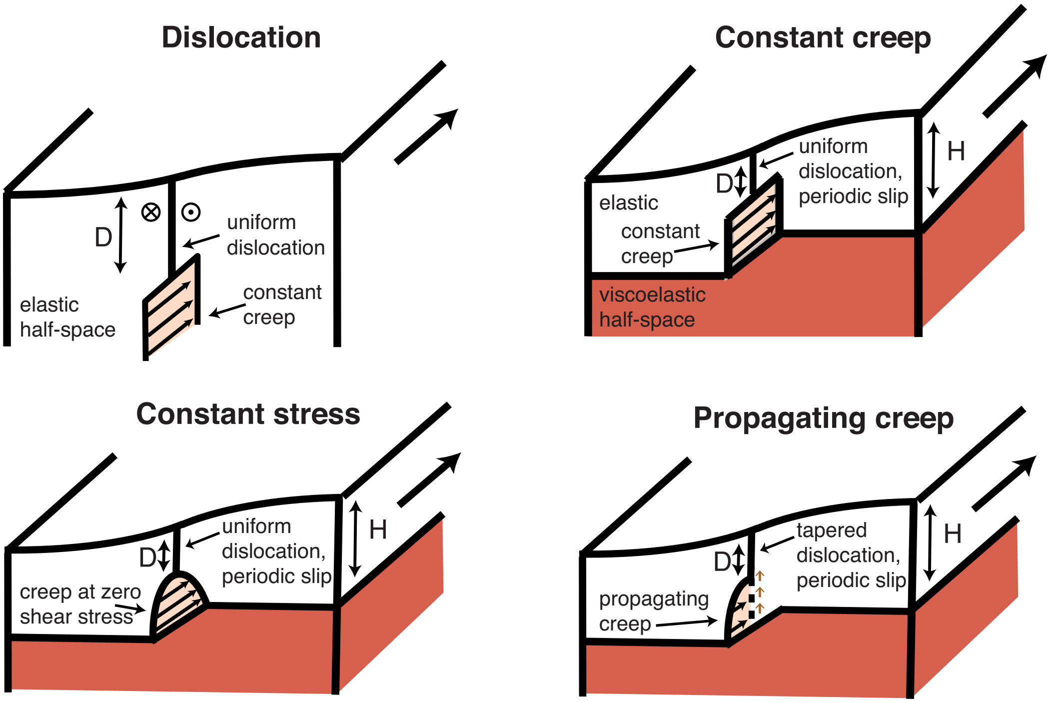

Figure 4. Models for interseismic creep considered in this study. Details are summarized in Table 2.

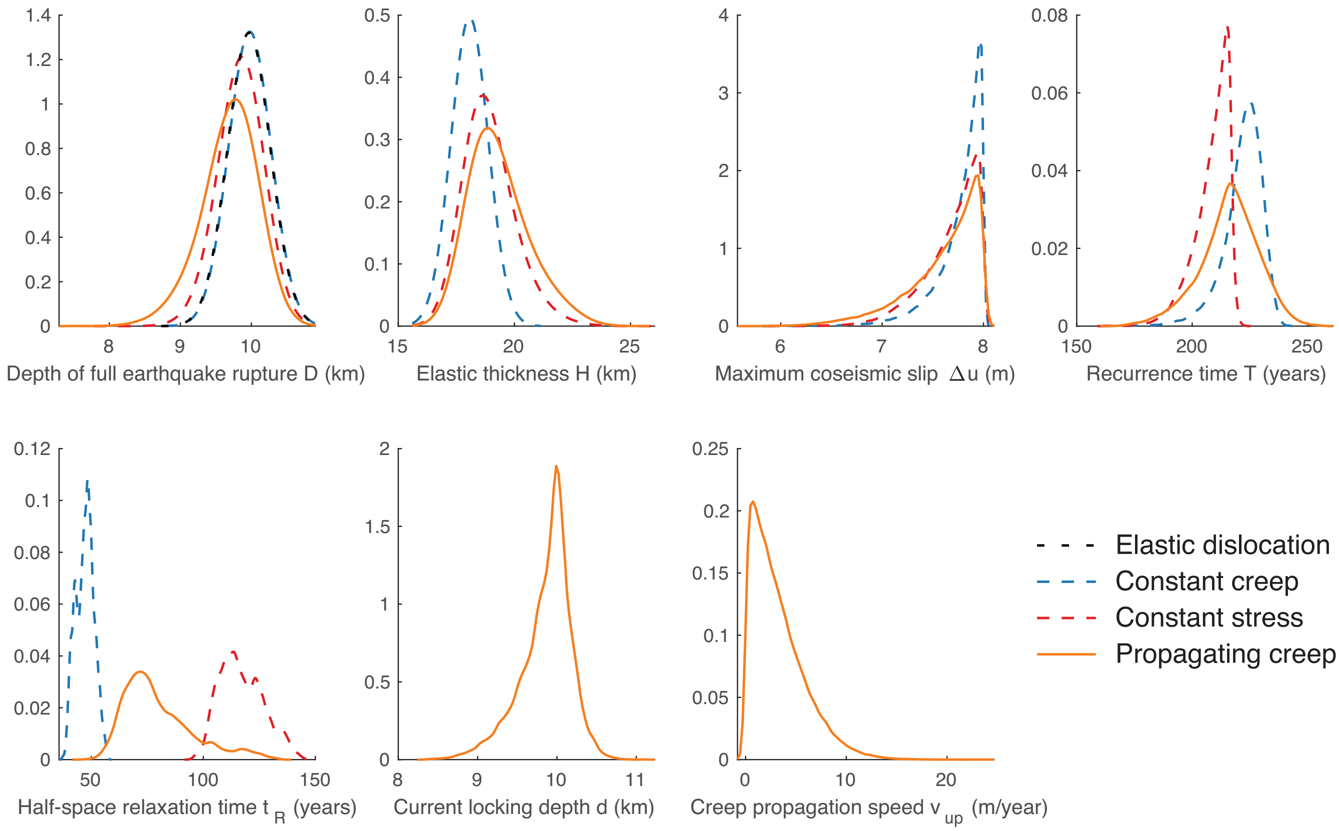

Figure 5. Posterior distributions for the depth of maximum coseismic slip D, the elastic thickness H, the amount of maximum coseismic slip Δu, the half-space relaxation time t_R, the recurrence time T, and, for this model specifically, the distribution of the current locking depth d and propagation speed of deep interseismic slip v_{up}. See Fig. 1 for a review of the different parameters.

vary between 0 and 8.5 m yr^{-1}. The relaxation time of the best-fitting solution lies at 70.2 yr, varying from 48.4 to 111.0. Fig. E2 presents the posterior distributions for parameters estimated in the propagating creep inversion, and the resulting propagation speed.

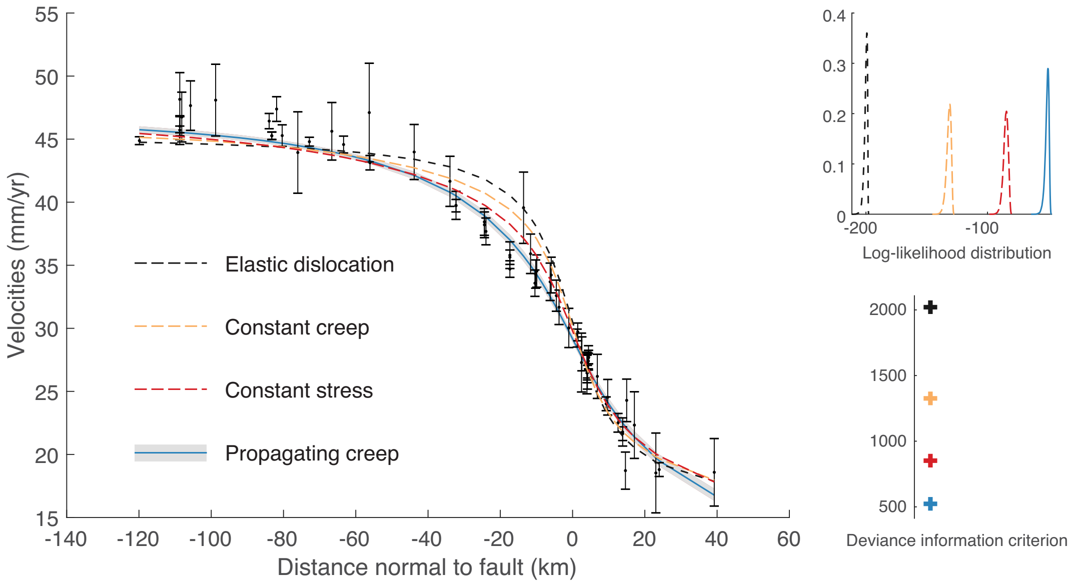

Figure 6. Best-fitting models, log-likelihood distributions and corresponding deviance information criteria. Although the difference is small, this propagating creep model fits better the data set compared to other models. Recall that the data were corrected for 3-D effect and the effect of the Hosgri fault.

Table 2. Inversion descriptions.

Type	Label	Description
Elastic	Dislocation	Single dislocation in elastic half-space
Viscoelastic	Constant creep	Model from Savage & Prescott (1978) Creeping region slipping at constant speed v^∞
Viscoelastic	Constant stress	Model from Johnson & Segall (2004) Creeping region slipping at constant resistive stress
Viscoelastic	Propagating creep	This study Creeping region migrating vertically

Table 3. Inversion results for all the tested models. Parameters with an asterisk are not inverted, but inferred using the relations given in Table 1.

Model	Dislocation		Constant creep		Constant stress		Propagating creep	
Parameter	Best fit	95% Conf.	Best fit	95% Conf.	Best fit	95% Conf.	Best fit	95% Conf.
D (km)	10.0	9.9–10.0	10.0	9.9–10.0	10.0	9.4–10.2	10.0	9.1–10.3
v^∞ (mm yr^{-1})	30.1	29.5–30.7	34.7	33.7–36.4	37.0	36.6–37.1	32.8	32.8–37.6
H (km)			18	17.9–18.2	18.0	17.6–19.4	18.2	17.1–21.5
t_R (yr)			45.5	39.2–55.0	101.0	99.8–118.4	70.2	48.4–111.0
Δu (m)			8.0	7.3–8.2	8.0	7.4–8.1	7.8	6.9–8.3
d (km)							10.0	9.2–10.5
H_{creep} (km)							18.2	15.6–21.3
T (yr)			230.5*	216.8–226.5*	215.0*	203.4–219.5*	234.0*	209.6–221.2*
T/t_R			5.1*	4.1–5.5*	2.1*	1.8–2.0*	3.3*	2.0–4.3*
v_{up} (m yr^{-1})							0.43*	0.0–8.5*

I observe a positive correlation between the relaxation time t_R, the elastic thickness H and the depth of constant creep H_{creep}. When focusing on the propagation speed v_{up}, there does not seem to be any strong correlation with the other inversion parameters. The sudden decrease in relaxation time between the model developed by Johnson & Segall (2004) and mine does not seem to be solely related to the addition of the propagating creep.

Although I found differences in parameters between the three viscoelastic earthquake cycle inversions, Fig. 6 shows that the differences in fit are limited. This improved model shows, however, a better range for the likelihood, compared to all other inversions. I also compute the deviance information criterion (DIC) (Spiegelhalter *et al.* 2002) to compare the fits. The deviance $D(m)$ is defined as

$$D(m) = -2\log[p(d|m)] + C, \tag{17}$$

where d is the data, m the unknown parameters, $p(y|m)$ the likelihood and C a constant that later cancels. The influence of the effective number of parameters is given by the difference between the expectation of the deviance $\bar{D}(m)$ and the deviance of the expectation of m:

$$p_D = \bar{D}(m) - D(\bar{m}). \tag{18}$$

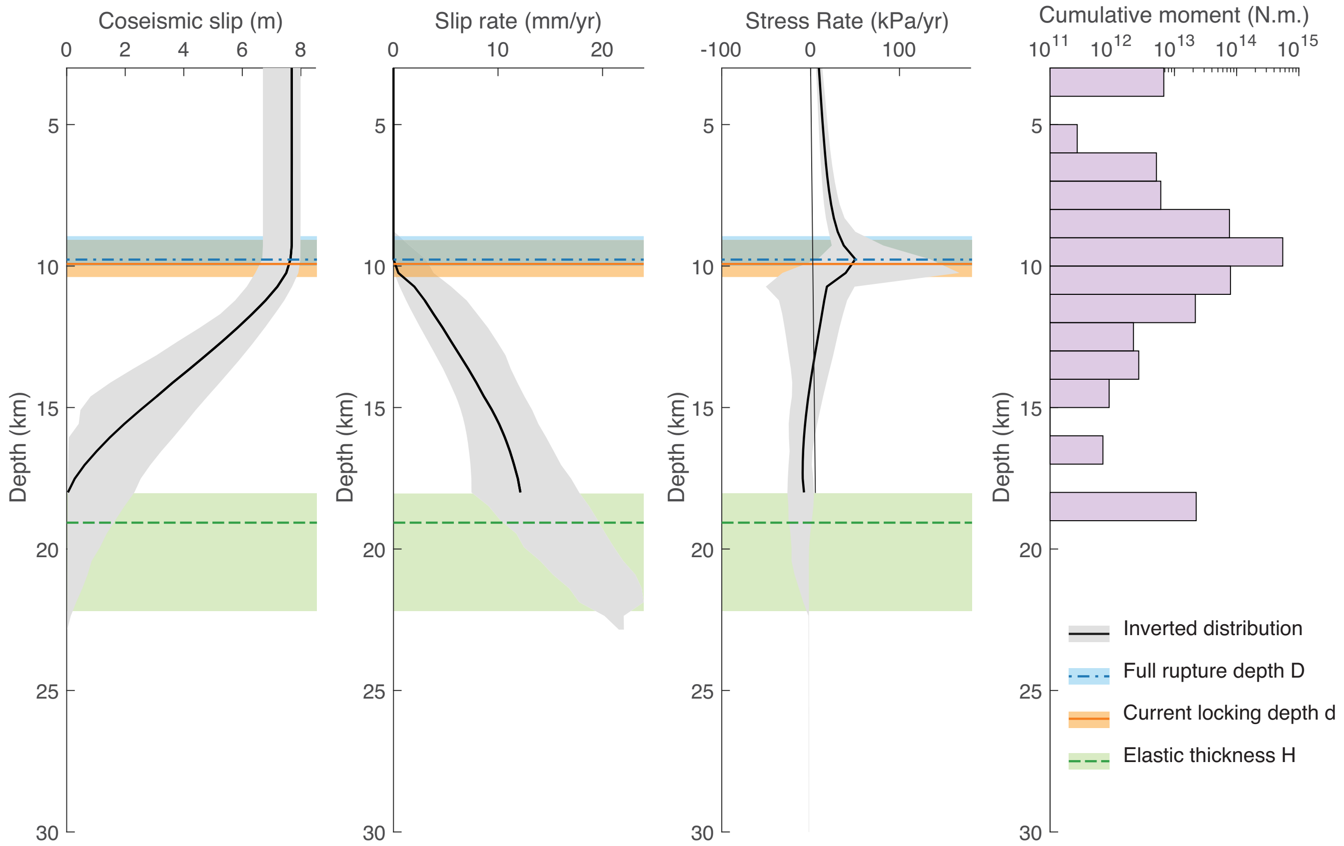

Figure 7. Distribution of coseismic slip, slip rate, stress rate, D, d and H for this improved model. Median solutions are indicated in bold lines, the 2σ uncertainties are given by the shaded regions. I compare the obtained stress rate distribution to the cumulative moment from microseismicity between 1981 and 2016 along the Carrizo Plain (Lin *et al.* 2007; Hauksson *et al.* 2012).

The DIC is then computed as followed:

$$\mathrm{DIC} = D(\bar{m}) + 2p_D. \tag{19}$$

The DIC is a way of measuring model fit, similar to Akaike information criterion (AIC), but for MCMC solutions. Models with lower DIC give the best estimated solutions. In this study, although I increased the number of parameters, my improved model has a DIC lower than all the other inversions, as shown in Fig. 6.

5 DISCUSSION

I investigated models that include viscoelastic flow and deep interseismic creep to explain the deformation rates across the Carrizo Plain section of the San Andreas fault. I improved the method developed by Bruhat & Segall (2017) to account for the coupling between the viscoelastic half-space and time-dependent interseismic creep. I propose a model with a coseismic region with constant coseismic slip down to 10 km, then slowly tapering down to 15–20 km (Fig. 7). The region of uniform coseismic rupture, down to $\approx$10 km is followed by a transitional region, where creep lies between the top of the viscoelastic layer and the apparent locking depth, and potentially can migrate vertically at speeds up to 10 m yr^{-1}. This model exhibits positive stress rate within the same region than the current microseismicity. This results show that this model might explain the surface rates across the Carrizo Plain section of the San Andreas fault.

Compared to the model with constant creep from Savage & Prescott (1978) and the boundary element model developed by Johnson & Segall (2004), I present a kinematic model that is much more efficient computationally and allow the spatial migration of the creeping region during the earthquake cycle. I derived analytical expressions for this to compute the viscoelastic response due to time-dependent creep. Although this model remains kinematic, it provides physical insights into the transitional region between the locked region and the top of the viscoelastic medium.

Note that the best-fitting solutions from this model have very low propagation speeds, less than a metre per year, as shown in Fig. 8, advocating for the lack of creep propagation. As a result, the difference in fit with the model developed by Johnson & Segall (2004) where creep occurs at constant creep, does not seem to be caused by the additional creep propagation. The model I developed, independently from the propagation, seems to provide a more flexible solution for creep rate distribution in the transitional region, leading to a systematic better fit.

All prior models assumed constant coseismic displacement along depth, meaning that the earthquake rupture would abruptly stop as it reaches the depth D. A sudden earthquake arrest is however probably unlikely. Most slip inversions assume spatial smoothing between patches of high and low slip for instance. The model I present here includes a more realistic transitional region below the depth of uniform rupture D. It allows the presence of a transitional region where tapered coseismic slip and migrating interseismic creep are colocated. Recent numerical studies have hinted the possibility for such deeper partial coseismic ruptures (Jiang & Lapusta 2016) due to enhanced weakening mechanisms. Although partial rupture add an extra degree of complexity when describing the transition between

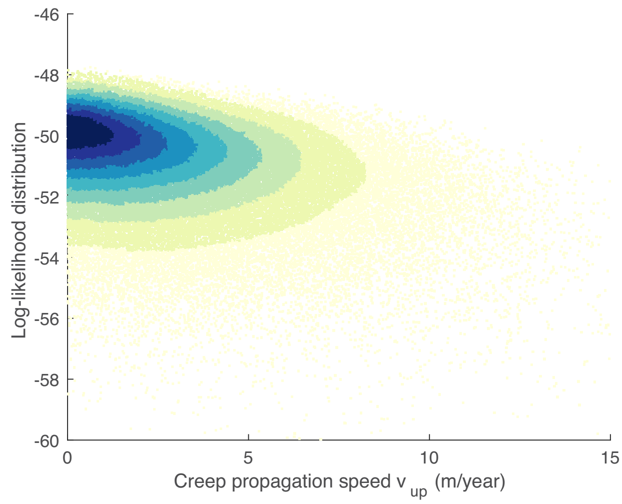

Figure 8. Density plot of the posterior distribution of the creep propagation speed against the log-likelihood. A lower log-likelihood indicates a better fit. In this inversion, while I allow the possibility for vertical migration of the locking depth, the best-fitting solutions converge towards a solution which is not migrating.

the locked and the creeping regions, such models improve significantly the physical representation of the transitional region and the overall fit, as shown in Fig. 6.

All the considered models assume an instantaneous characteristic rupture every T years. Although, the cumulative response of the underneath viscoelastic medium to each characteristic earthquake is acknowledged, most of them neglect time-dependent afterslip and more generally post-seismic deformation. Post-seismic slip could account for a significant part of the slip happening within the creeping region. Only the boundary element model developed by Johnson & Segall (2004) considered instantaneous slip in the region between D and H, which might be assimilated as a partial deep rupture, but does not evolve with time. As the deep region of the elastic layer slips post-seismically, it also feeds and amplifies the response of the viscoelastic medium. This additional time-dependent behaviour from the post-seismic response is completely ignored in any of this viscoelastic modelling.

The variability of the typical-earthquake characteristics might also affect the long-term viscoelastic cycle model. Although the San Andreas Fault has been quiet in this region since 1857, paleoseismic studies have shown that most precedent events displayed lower surface-breaking displacements, as well as shorter recurrence time intervals (Akciz *et al.* 2009, 2010; Scharer *et al.* 2014) These studies suggest that there is no 'characteristic' earthquake along the Carrizo Plain segment, and that, as a result, the 1857 event might be a rare larger event. Note that the corollary would also suggest smaller coseismic displacements in the geodetic inversions.

Nevertheless, I developed a model that allows crack propagation that considers the coupling between the viscoelastic half-space and the creeping region. In particular, I extended the models from Bruhat & Segall (2017) to compute viscoelastic surface rates caused by time-dependent slip rates along the fault. Using this improved model, I found solutions for fitting the surface deformation rates that allow for reasonable estimates for earthquake rupture depth and coseismic displacement. Above the viscoelastic half-space, deep interseismic slip might be migrating vertically at rates up to 10 m yr^{-1}, slowly unlocking the deepest region of the elastic crust. I present a model that could be used as a first step to explain the discrepancy between geodetically derived locking depths and microseismicity along the San Andreas fault. The observation of deep microseismicity and tremors suggests indeed that there is at least some fault slip well below the nominally locked part of the fault (Nadeau & Guilhem 2009; Shelly 2010). However, since the propagation velocity is very small, less than 1 km in 100 yr, it is highly likely that the creep migration, if real, could not be currently detected given the geodetic data temporal span and the still large uncertainties on the locking depth along the San Andreas fault.

Likewise, I tested this method on a simple data set that used averaged temporal deformation. The addition of a possible time-dependent behaviour calls for the use of time-dependent data, that would highlight the characteristics of migrating speed. Future work should consider the use of additional data sets, such as microseismicity, repeating earthquakes, and tremor locations, to study and better constrain this behaviour in fault systems. As observations of time-dependent deformation during the interseismic period, or even before large events, become more common, this type of inversion method would become more and more necessary.

While this study focused on the Carizzo plain section of the San Andreas fault, the approach could be easily expended to other strike-slip faults. Current work on the North Anatolian fault have shown for instance that the long-term deformation rates seem constant through the interseismic period, which could suggest the lack of migrating creep (Hussain *et al.* 2018). The study from Jiang & Lapusta (2016), which actually first mentioned the possibility of a migrating locking depth, looked at microseismicity pattern in large strike-slip fault segments to estimate whether the locking depth could have been pushed further at depth after large earthquakes. These locations could serve as starting point for further evaluating deep interseismic creep.

The first and most obvious application of my method is to provide a physics-based tool for kinematic inversions that remains simple to use, but still allows vertical migration of the creeping region in a viscoelastic earthquake cycle modelling. Nonetheless, this method could also be used as a verification tool for more elaborated physics-based fully-numerical modelling. While I recognize that dividing the crust in a elastic medium of constant elastic moduli overlying a viscoelastic half-space remains a simple model that strongly differs with recent physically motivated models (e.g. Takeuchi & Fialko 2012; Hearn & Thatcher 2015; Lambert & Barbot 2016; Allison & Dunham 2018; Zhang & Sagiya 2018), such methods for modelling the crust are still wildly used in kinematic inversions. Results from fully-numerical models should be verified against various approach of kinematic inversions, such as the one developed here. For instance, when Allison & Dunham (2018) finds that even the brittle–ductile transition evolves with cumulative earthquake cycle, it would be really interesting to invert the surface deformation rates they produce with the method I developed here. As screw dislocation arctangents remain still fairly ubiquitous (Meade *et al.* 2013; Wright *et al.* 2013), being able to pinpoint the components of interseismic deformation rates to actual physical characteristics using knowledge from both the kinematic inversions and the fully-numerical models would be an encouraging step forward.

ACKNOWLEDGEMENTS

I would like to thank Paul Segall for discussions and guidance through this work, and Kaj Johnson for providing me his viscoelastic code. I also thank the editor Eiichi Fukuyama, Tim

Wright and an anonymous reviewer for their constructive comments. This work was supported by the Southern California Earthquake Center (Award #17136). GPS rates were provided by the SCEC Crustal Motion Model Map (Shen *et al.* 2011) and are available at http://scec.ess.ucla.edu/∼zshen/cmm4/cmm4.html. Codes for crack and viscoelastic modelling are available on https://github.com/lucilebruhat/.

REFERENCES

Akciz, S.O., Grant Ludwig, L. & Arrowsmith, J.R., 2009. Revised dates of large earthquakes along the Carrizo section of the San Andreas Fault, California, since A.D. 1310 30, *J. geophys. Res.,* **114**(B1), B01313.

Akciz, S.O., Ludwig, L.G., Arrowsmith, J.R. & Zielke, O., 2010. Century-long average time intervals between earthquake ruptures of the San Andreas fault in the Carrizo Plain, California, *Geology,* **38**(9), 787–790.

Allison, K.L. & Dunham, E.M., 2018. Earthquake cycle simulations with rate-and-state friction and power-law viscoelasticity, *Tectonophysics,* **733,** 232–256.

Bilby, B.A. & Eshelby, J.D., 1968. Dislocations and the theory of fracture, in *Fracture, An Advanced Treatise,* pp. 99–182, Academic Press.

Bruhat, L. & Segall, P., 2017. Deformation rates in northern cascadia consistent with slow up dip propagation of deep interseismic creep, *Geophys. J. Int,* **211**(1), 427–449.

Dragert, H., 2001. A silent slip event on the deeper cascadia subduction interface, *Science,* **292**(5521), 1525–1528.

Field, E.H. *et al.*, 2014. Uniform California earthquake rupture forecast, version 3 (UCERF3)–the time-independent model, *Bull. seism. Soc. Am.,* **104**(3), 1122–1180.

Flück, P., Hyndman, R.D. & Wang, K., 1997. Three-dimensional dislocation model for great earthquakes of the Cascadia Subduction Zone, *J. geophys. Res.,* **102**(B9), 20539.

Hardebeck, J.L., 2010. Seismotectonics and fault structure of the California Central coast, *Bull. seism. Soc. Am.,* **100**(3), 1031–1050.

Hauksson, E., Yang, W. & Shearer, P.M., 2012. Waveform relocated earthquake catalog for Southern California (1981 to June 2011), *Bull. seism. Soc. Am.,* **102**(5), 2239–2244.

Hearn, E.H. & Thatcher, W.R., 2015. Reconciling viscoelastic models of postseismic and interseismic deformation: effects of viscous shear zones and finite length ruptures, *J. geophys. Res.,* **120**(4), 2794–2819.

Hetland, E.A. & Simons, M., 2010. Post-seismic and interseismic fault creep II: transient creep and interseismic stress shadows on megathrusts, *Geophys. J. Int.,* **181**(1), 99–112.

Hetland, E.A., Simons, M. & Dunham, E.M., 2010. Post-seismic and interseismic fault creep I: model description, *Geophys. J. Int.,* **181**(1), 81–98.

Hussain, E., Wright, T.J., Walters, R.J., Bekaert, D.P.S., Lloyd, R. & Hooper, A., 2018. Constant strain accumulation rate between major earthquakes on the North Anatolian Fault, *Nat. Commun.,* **9**(1), 1392.

Jiang, J. & Lapusta, N., 2016. Deeper penetration of large earthquakes on seismically quiescent faults, *Science,* **352**(6291), 1293–1297.

Johnson, K.M., 2013. Slip rates and off-fault deformation in Southern California inferred from GPS data and models, *J. geophys. Res.,* **118**(10), 5643–5664.

Johnson, K.M. & Segall, P., 2004. Viscoelastic earthquake cycle models with deep stress-driven creep along the San Andreas fault system, *J. geophys. Res.,* **109**(B10), doi:10.1029/2004JB003096.

Johnson, K.M., Mavrommatis, A. & Segall, P., 2016. Small interseismic asperities and widespread aseismic creep on the northern Japan subduction interface, *Geophys. Res. Lett.,* **43**(1), 135–143.

Johnson, S.Y. & Watt, J.T., 2012. Influence of fault trend, bends, and convergence on shallow structure and geomorphology of the Hosgri strike-slip fault, offshore central California, *Geosphere,* **8**(6), 1632–1656.

Johnson, S.Y., Hartwell, S.R. & Dartnell, P., 2014. Offset of latest pleistocene shoreface reveals slip rate on the Hosgri strike-slip fault, offshore Central California, *Bull. seism. Soc. Am.,* **104**(4), 1650–1662.

Lambert, V. & Barbot, S., 2016. Contribution of viscoelastic flow in earthquake cycles within the lithosphere-asthenosphere system, *Geophys. Res. Lett.,* **43**(19), 10142–10 154.

Lin, G., Shearer, P.M. & Hauksson, E., 2007. Applying a three-dimensional velocity model, waveform cross correlation, and cluster analysis to locate southern California seismicity from 1981 to 2005, *J. geophys. Res.,* **112**(B12), B12309.

Mavrommatis, A.P., Segall, P. & Johnson, K.M., 2014. A decadal-scale deformation transient prior to the 2011 Mw 9.0 Tohoku-oki earthquake, *Geophys. Res. Lett.,* **41**(13), 4486–4494.

Mavrommatis, A.P., Segall, P. & Kaj, J., 2017. A physical model for interseismic erosion of locked fault asperities, *J. geophys. Res.,* **122**(10), 8326–8346.

Meade, B.J., Klinger, Y. & Hetland, E.A., 2013. Inference of multiple earthquake-cycle relaxation timescales from irregular geodetic sampling of interseismic deformation, *Bull. seism. Soc. Am.,* **103**(5), 2824–2835.

Nadeau, R.M. & Guilhem, A., 2009. Nonvolcanic tremor evolution and the San Simeon and Parkfield, California, earthquakes, *Science,* **325**(5937), 191–193.

Noriega, G.R., Arrowsmith, J.R., Grant, L.B. & Young, J.J., 2006. Stream channel offset and late holocene slip rate of the San Andreas fault at the Van Matre Ranch Site, Carrizo Plain, California, *Bull. seism. Soc. Am.,* **96**(1), 33–47.

Obara, K., 2002. Nonvolcanic deep tremor associated with subduction in southwest Japan, *Science,* **296**(5573), 1679–81.

Savage, J. & Burford, R., 1970. Accumulation of tectonic strain in California, *Bull. seism. Soc. Am.,* **60**(6), 1877–1896.

Savage, J.C., 1990. Equivalent strike-slip earthquake cycles in half-space and lithosphere-asthenosphere earth models, *J. geophys. Res.,* **95**(B4), 4873–4879.

Savage, J.C. & Prescott, W.H., 1978. Asthenosphere readjustment and the earthquake cycle, *J. geophys. Res.,* **83**(B7), 3369–3376.

Scharer, K., Weldon, R., Streig, A. & Fumal, T., 2014. Paleoearthquakes at Frazier Mountain, California delimit extent and frequency of past San Andreas Fault ruptures along 1857 trace, *Geophys. Res. Lett.,* **41**(13), 4527–4534.

Segall, P., 2010. *Earthquake and Volcano Deformation,* Princeton Univ. Press.

Segall, P. & Bradley, A.M., 2012. Slow-slip evolves into megathrust earthquakes in 2D numerical simulations, *Geophys. Res. Lett.,* **39**(18), 308.

Seno, T., 2003, Fractal asperities, invasion of barriers, and interplate earthquakes, **55,** 649–665.

Shelly, D.R., 2010. Periodic, chaotic, and doubled earthquake recurrence intervals on the deep San Andreas fault, *Science,* **328**(5984), 1385–1388.

Shen, Z.-K., King, R.W., Agnew, D.C., Wang, M., Herring, T.A., Dong, D. & Fang, P., 2011. A unified analysis of crustal motion in Southern California, 1970-2004: the SCEC crustal motion map, *J. geophys. Res.,* **116**(B11), doi:10.1029/2011JB008549.

Sieh, K.E., 1978. Slip along the San Andreas fault associated with the great 1857 earthquake, *Bull. seism. Soc. Am,* **68**(5), 1421–1448.

Smith-Konter, B.R., Sandwell, D.T. & Shearer, P., 2011. Locking depths estimated from geodesy and seismology along the San Andreas Fault System: implications for seismic moment release, *J. geophys. Res.,* **116**(B6), B06401.

Spiegelhalter, D.J., Best, N.G., Carlin, B.P. & van der Linde, A., 2002. Bayesian measures of model complexity and fit, *J. R. Stat. Soc., B,* **64**(4), 583–639.

Takeuchi, C.S. & Fialko, Y., 2012. Dynamic models of interseismic deformation and stress transfer from plate motion to continental transform faults, *J. geophys. Res.,* **117**(B5), doi:10.1029/2011JB009056.

Wright, T.J., Elliott, J.R., Wang, H. & Ryder, I., 2013. Earthquake cycle deformation and the Moho: implications for the rheology of continental lithosphere, *Tectonophysics,* **609,** 504–523.

Zhang, X. & Sagiya, T., 2018. Intraplate strike-slip faulting, stress accumulation, and shear localization of a crust-upper mantle system with nonlinear viscoelastic material, *J. geophys. Res.,* **123**(10), 9269–9285.

Zielke, O., Arrowsmith, J.R., Ludwig, L.G. & Akciz, S.O., 2010. Slip in the 1857 and earlier large earthquakes along the Carrizo Plain, San Andreas Fault, *Science,* **327**(5969), 1119–1122.

APPENDIX A: VISCOELASTIC STRESSES CAUSED BY REPEATED SLIP IN THE SEISMOGENIC REGION

Stress rates are obtained by computing the strain rates using velocities given in eq. (2) and applying Hooke's law (Johnson & Segall 2004). Stresses are then derived by integrating over the duration of the time interval T. The expression for stress at the location (x_k, z_k) due to slip δ_i at depth z_i is

$$\sigma_i(x_k, z_k, t) = \delta_i \frac{\mu}{2\pi}\frac{T}{t_R} e^{-t/t_R} \sum_{n=1}^{\infty} \frac{W_n(x_k, z_k, z_i, H)}{(n-1)!} \times \sum_{k=0}^{K} e^{-kT/t_R} \left(\frac{t+kT}{t_R}\right)^{n-1}, \tag{A1}$$

using the spatial operator W_n:

$$W_n(x_k, z_k, z_i, H) = V_n(x_k, z_k, z_{i+1}, H) - V_n(x_k, z_k, z_i, H), \tag{A2a}$$

where

$$V_n(x_k, z_k, z_i, H) = -\frac{z_k - 2nH + z_i}{(z_k - 2nH + z_i)^2 + x_k^2} + \frac{z_k - 2nH - z_i}{(z_k - 2nH - z_i)^2 + x_k^2} \tag{A2b}$$

$$+\frac{z_k + 2nH + z_i}{(z_k + 2nH + z_i)^2 + x_k^2} - \frac{z_k + 2nH - z_i}{(z_k + 2nH - z_i)^2 + x_k^2}. \tag{A2c}$$

For points on the fault, $x_k = 0$ and V_n simplifies to:

$$V_n(z_k, z_i, H) = -\frac{1}{z_k - 2nH + z_i} + \frac{1}{z_k - 2nH - z_i} + \frac{1}{z_k + 2nH + z_i} - \frac{1}{z_k + 2nH - z_i}. \tag{A3}$$

APPENDIX B: GENERALIZED EQUATIONS FOR CRACK MODEL

Following Bilby & Eshelby (1968), the stress drop within the crack can be expanded in Chebyshev polynomials of the first kind T_i:

$$\Delta\tau(u) = \mu \sum_{i=0}^{\infty} c_i T_i(u). \tag{B1}$$

Bruhat & Segall (2017) showed that for a non-singular crack, that is with finite stress at the crack tip and driven by steady displacement δ^∞, $c_0 = 0$ and $c_1 = 2\delta^\infty/a\pi$. This leads to the following expressions for stress drop within the crack and slip:

$$\Delta\tau(\xi, t) = \mu \frac{2\delta^\infty}{a\pi}\xi + \mu \sum_{i=2}^{\infty} c_i T_i(\xi), \tag{B2}$$

$$s(\xi, t) = \frac{\delta^\infty}{\pi}\left[\xi\sqrt{1-\xi^2} + \arcsin(\xi) + \frac{\pi}{2}\right] + \frac{a}{2}\sqrt{1-\xi^2}\sum_{i=2}^{\infty} c_i \left[\frac{U_i(\xi)}{i+1} - \frac{U_{i-2}(\xi)}{i-1}\right], \tag{B3}$$

where U_i are Chebyshev polynomials of the second kind.

Finally, taking the total derivative of $s(\xi, t)$ to get slip-rate, I find

$$\frac{ds}{dt}(\xi, t) = \dot{\delta}^\infty g + \frac{a}{2}\sum_{i=2}^{\infty}\frac{dc_i}{dt} f_i + \frac{da}{dt}\left[g'\frac{1-\xi}{a}\delta^\infty + \sum_{i=2}^{\infty}\frac{c_i}{2}\left(f_i + f_i'(1-\xi)\right)\right], \tag{B4}$$

where

$$f_i = \sqrt{1-\xi^2}\left[\frac{U_i}{i+1} - \frac{U_{i-2}}{i-1}\right], \tag{B5a}$$

$$f_i' = 2\sqrt{1-\xi^2}U_{i-1}, \tag{B5b}$$

$$g = \frac{1}{\pi}\left[\xi\sqrt{1-\xi^2} + \arcsin\xi + \frac{\pi}{2}\right], \tag{B5c}$$

$$g' = \frac{2}{\pi}\sqrt{1-\xi^2}. \tag{B5d}$$

APPENDIX C: TIME-DEPENDENT DISPLACEMENT CONDITION AT THE DOWNDIP LIMIT OF THE CRACK

Bruhat & Segall (2017) considered that the displacement at the downdip extent of the crack was constant through time, and equals to the long-term rate v^∞. Indeed, they considered a crack in a elastic half-space, loading by constant creep. In this study, due to the presence of a viscoelastic half-space below the elastic crust, the values of this boundary condition for slip and slip rate must match the motion of the viscoelastic half-space, that is an initial loading due to an earthquake on the shallower fault, followed by time-dependent relaxation. I here derive the boundary conditions $\dot{\delta}^\infty(t)$ and δ^∞(t) such that they follow the time-dependent motion of the shallowest point of the viscoelastic half-space.

Following Savage & Prescott (1978) (also given in eqs (12.20)–(12.26) from Segall (e.g. 2010, section 12.4.1), the horizontal velocity at the free surface due to the cumulative effect of cumulative effect of N regularly spaced earthquakes is given by

$$v(x, t) = \frac{1}{\pi}\sum_{n=1}^{\infty}\mathcal{T}_n(t/t_R, T/t_R)\mathcal{F}_n(x, D, H), \tag{C1}$$

where

$$\mathcal{T}_n(t/t_R, T/t_R) = \frac{v^\infty T}{t_R}\frac{e^{-t/t_R}}{(n-1)!}\sum_{k=0}^{N} e^{-kT/t_R}\left(\frac{t+kT}{t_R}\right)^{n-1}. \tag{C2}$$

The time-dependence is then given by the term $\mathcal{T}_n(t/t_R, T/t_R)$, where each mode as an exponential character. Savage (1990) noted that the viscoelastic solution given above is mathematically equivalent to fault slip within an elastic half-space in a series of strips at depths H, $3H$, ... below the coseismic region. Since the crack bottom end lies at the upper limit of the viscoelastic medium, the bottom velocity condition $\dot{\delta}^\infty(t)$ corresponds to the velocity of the viscoelastic region at its upper end. The velocity of this point is then directly given by the summation of $\mathcal{T}_n$ as n goes from 1 to infinity.

Savage (1990) also showed that this summation quickly approaches the long-term rate v^∞ with increasing n. Instead of using the full summation, I approximate $\dot{\delta}^\infty(t)$ by only considering the first two nodes $\mathcal{T}_n$ from the previous equation. For a large number of earthquakes N in (C.2), $\dot{\delta}^\infty(t)$ can be rewritten as:

$$\dot{\delta}^{\infty}(t) = \frac{1}{2}\left[\mathcal{T}_1(t/t_R, T/t_R) + \mathcal{T}_2(t/t_R, T/t_R)\right] \tag{C3}$$

$$= \frac{v^{\infty}T}{2t_R} e^{-t/t_R}\left(\frac{e^{-T/t_R}}{e^{-T/t_R}-1}\right)\left[1 + \frac{t}{t_R} + \frac{T}{t_R}\left(\frac{1}{e^{-T/t_R}-1}\right)\right]. \tag{C4}$$

Finally, I compute the condition δ^{∞}(t) by numerical integration:

$$\delta^{\infty}(t) = \frac{1}{2}\int_0^t \left[\mathcal{T}_1(t/t_R, T/t_R) + \mathcal{T}_2(t/t_R, T/t_R)\right] \mathrm{d}t. \tag{C5}$$

Obviously, I make an approximation of the velocity at the elastic-viscoelastic limit by using the first two nodes of the equivalent slip model from Savage (1990). While this approximation produces the same surface deformation pattern than Savage & Prescott (1978), it does not reproduce the actual internal deformation at the elastic-viscoelastic limit. Because I focus in this study at developing a simple kinematic model that considers time dependent interseismic creep to fit surface rates, this approximation will be enough at this stage of modelling. The time dependency of the new boundary condition is the critical point here, as it will affect the shape of the creeping crack, and the resulting surface deformation pattern.

APPENDIX D: EVALUATION OF CREEP-INDUCED VISCOELASTIC EFFECTS

In this section, I verify the method that I developed in Section 2.3 against previous codes for creep-induced viscoelastic effects. I make use of earthquake cycle models developed by Johnson & Segall (2004) to compute slip-rate profiles for interseismic creep. This model assumes that the region between D and H is unlocked, is fixed in length during the interseismic period, and slips at constant resistive shear stress. The solution for slip and slip rate within the creeping region is then computed through a boundary element approach.

First, I use profiles of surface rates and slip rates within the creeping region using the approach from Johnson & Segall (2004) to estimate the portion of surface deformation attributed to creep-induced viscoelastic response. For a given set of input parameters: rupture depth D, elastic thickness H, relaxation time t_R, recurrence time T and plate motion velocity v^{∞}, I produce profiles of surface rates and interseismic slip rates. Here I use $D = 15$ km, $H = 30$ km, $T = 300$ yr, $v^{\infty} = 3$ cm yr^{-1}. Deformation profiles for two relaxation times t_R are displayed in Fig. D1. Left-hand panels show profiles for surface rates and slip rates in the creeping region at 10 time intervals during the interseismic period. These profiles are computed using codes from Johnson & Segall (2004). Top middle panel gives surface rates due to periodic earthquake rupturing from the surface to depth D every T years. These are computed using analytical solution for earthquake cycle models (as in Segall 2010, section 12.4.2). Bottom middle panel displays elastic deformation rates caused by interseismic creep. These surface rates relate to the slip rates displayed in the bottom left-hand panel via elastic Green's functions.

Right-hand panels display the viscoelastic deformation as a function of time, and space, due to time-varying slip rate profiles shown in the bottom left-hand panel. These profiles result from the subtraction of the coseismic cycle deformation and the elastic deformation

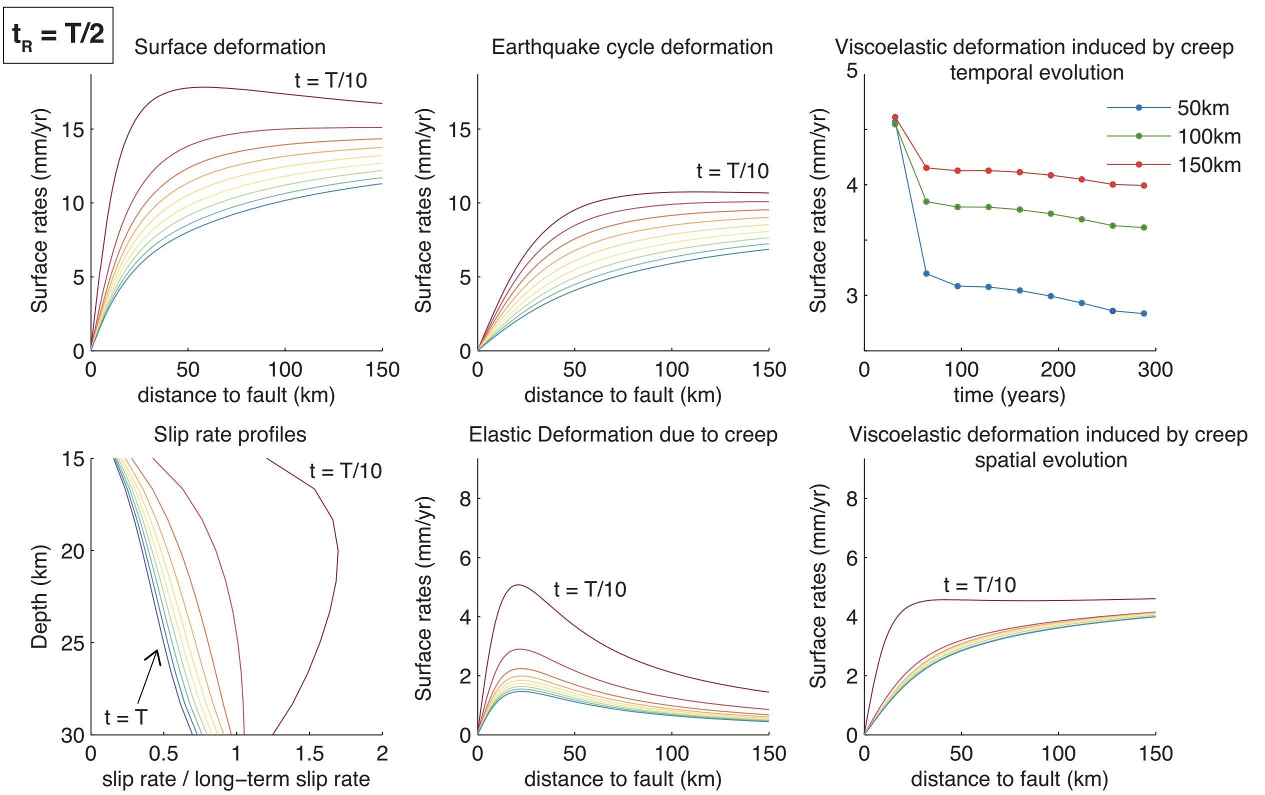

Figure D1. Estimation of viscoelastic deformation induced by time-varying creep when $t_R = T/2$. Left-hand panel: profiles for surface rates and slip rates from Johnson & Segall (2004). Top middle: surface rates due to cyclic earthquake ruptures. Bottom middle: elastic rates caused by interseismic creep. Right-hand panel: viscoelastic deformation as a function of time, and space, caused by slip rates in bottom left-hand panel.

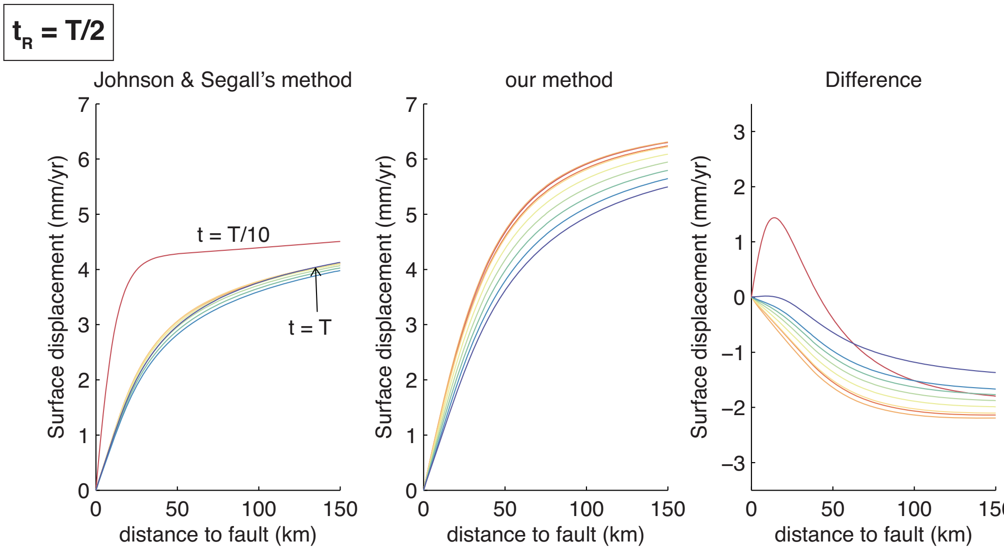

Figure D2. Surface predictions of viscoelastic deformation induced by time-varying creep using the method developed by Johnson & Segall (2004) and ours. The recurrence time is $T = 300$ yr, $t_{\mathrm{R}} = T/2$, and the number of time increments is 10.

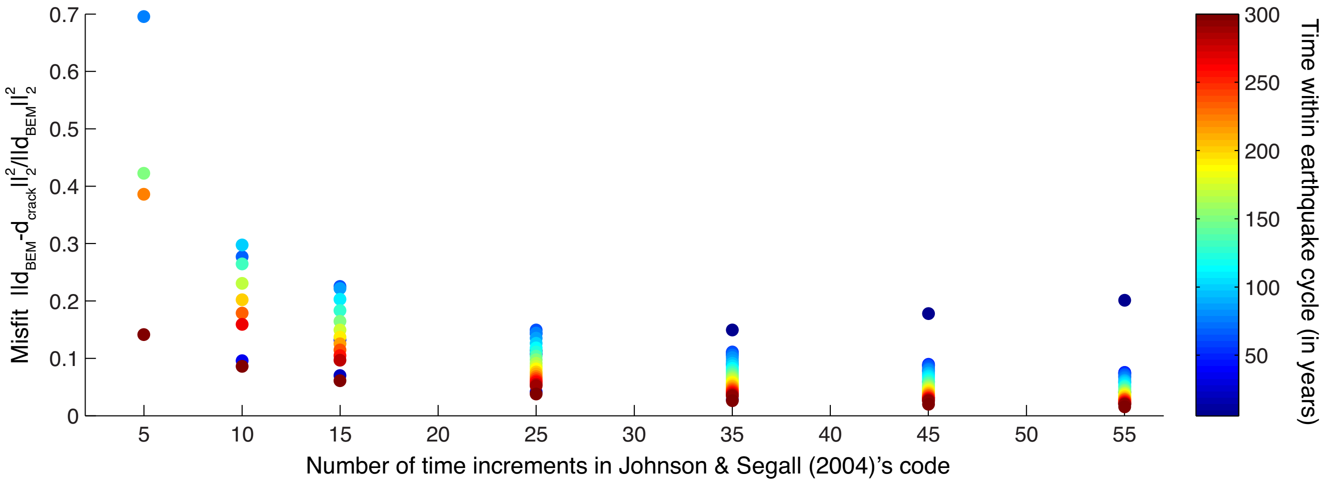

Figure D3. Comparison between the surface prediction of viscoelastic deformation induced by time-varying creep from Johnson & Segall (2004) (d_{BEM}) and this method (d_{crack}) as a function of the time discretization used in the boundary element code and time. The recurrence time is $T = 300$ yr and $t_{\mathrm{R}} = T/2$.

caused by creep, both displayed in middle panels, from the original surface deformation shown in the top left-hand panel. Fig. D1 shows that the surface deformation is dominated by the earthquake cycle signal, up to 70 per cent of the signal. The amplitude of the elastic and viscoelastic deformation pattern are roughly similar, each accounting for 10–20 per cent of the total rates. However, note the different evolution, as the elastic deformation decreases both temporally and spatially, while the viscoelastic response reaches an asymptotic trend which increases with distance from the fault. The viscoelastic signal will dominate especially late in the earthquake cycle. Since the viscoelastic effect of interseismic creep is comparable to the elastic part, I cannot neglect the effect of viscoelastic flow in the surface rates.

Now, I compare the viscoelastic response induced by creep from Johnson & Segall (2004) with this model. I use the slip rate profiles of creep from Johnson & Segall (2004), considering 10 time increments, and compute the surface deformation from the viscoelastic response using eq. (14, see Fig. D2). This method reproduces the overall shape and amplitude of the surface rates, especially late in the earthquake cycle. As I only use 10 increments in Johnson & Segall (2004)'s model, which is the number of time increment used in the original paper, I now test the effect of increasing the number of time increments.

Fig. D3 displays the misfit between the surface prediction from Johnson & Segall (2004) and this method as a function of the time discretization used in the boundary element code and time within the earthquake cycle. I show that the difference between the two methods decreases with finer discretization. The main difference lies in the earliest computed time. This corresponds to the instantaneous coseismic deformation in the creeping response, that appears in Johnson & Segall (2004)'s method, but not in mine. When used for later periods in the earthquake cycle, I conclude that this method is adequate enough to reproduce viscoelastic response induced by time-dependent creep. Obviously, one could advocate for using the method developed by Johnson & Segall (2004) with 10 and more time increments, but at that point the method becomes actually too computationally expensive to use in a MCMC context.

APPENDIX E: 3-D EFFECTS

I use the kinematic block model developed by Johnson (2013) to compute 2-D synthetic data along a line perpendicular to the Carrizo Plain section of the San Andreas fault (see Fig. E1). This model considers the entire extent of the San Andreas fault in Central and Southern California. I assume the San Andreas fault locked up to 19 km (Smith-Konter *et al.* 2011) and fully creeping in the northern creeping section. Using the surface rates due to an infinitely long fault also locked at 19 km, I compute the difference between the 1-D and the 2-D models that I considered as a correction to the surface rates. Corrected data are displayed in Fig. 1.

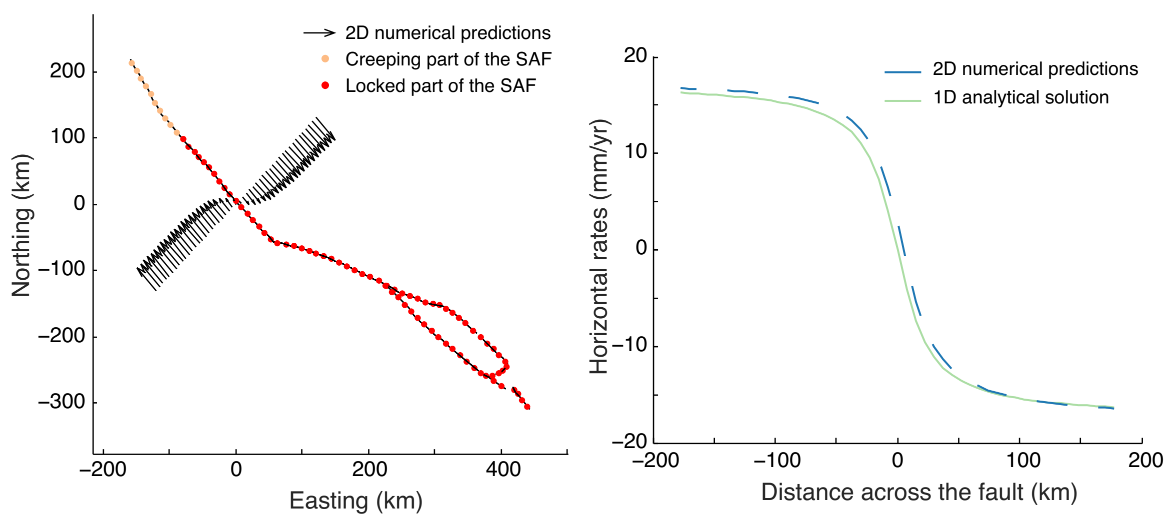

Figure E1. Estimation of 3-D effects (locking depth is 19 km).

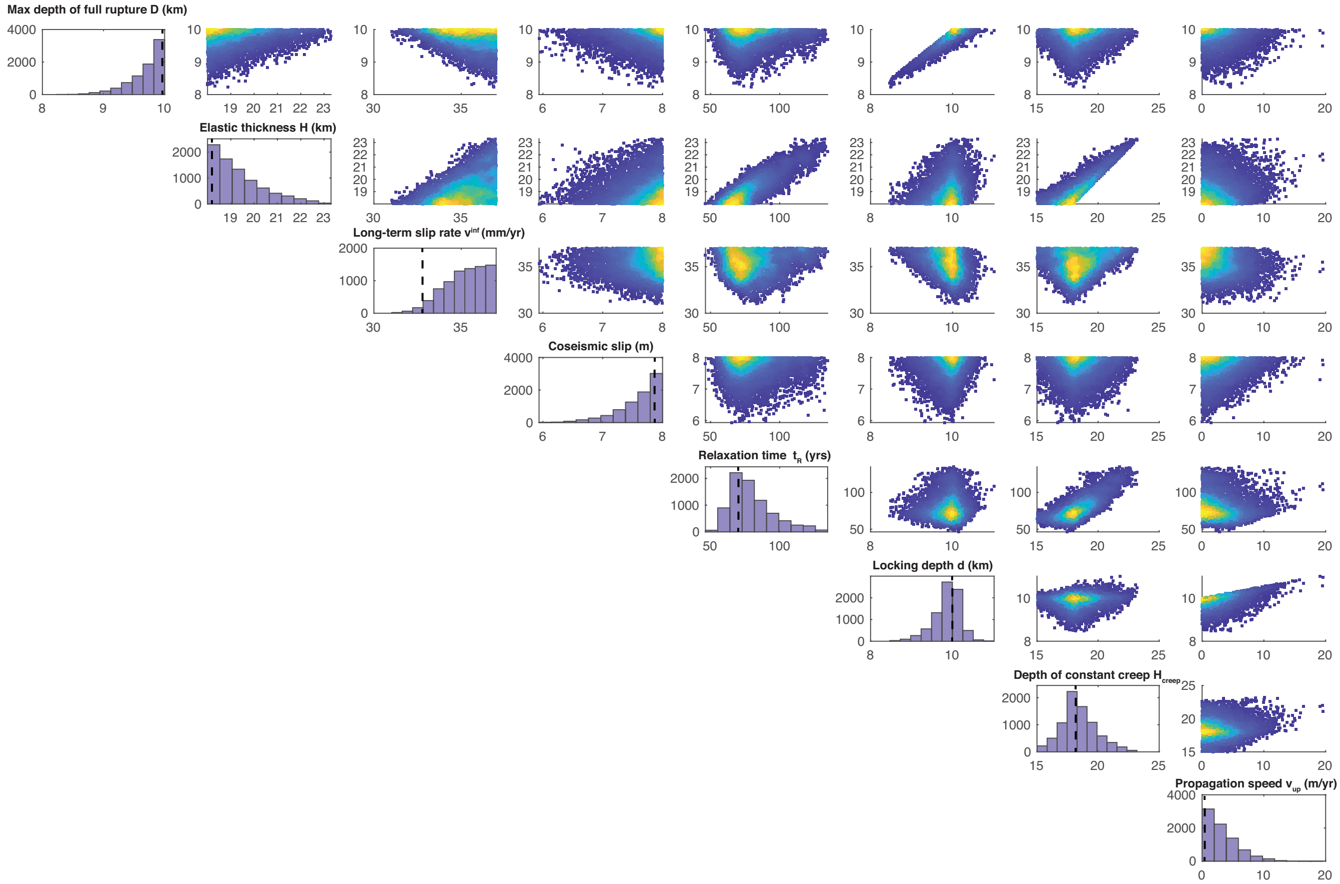

Figure E2. Marginal posterior distributions for parameters estimated in the propagating creep inversion. Best-fitting solution are indicated by the dashed black lines.

Key words

Authors are requested to choose key words from the list below to describe their work. The key words will be printed underneath the summary and are useful for readers and researchers. Key words should be separated by a semi-colon and listed in the order that they appear in this list. An article should contain no more than six key words.

COMPOSITION and PHYSICAL PROPERTIES
Composition and structure of the continental crust
Composition and structure of the core
Composition and structure of the mantle
Composition and structure of the oceanic crust
Composition of the planets
Creep and deformation
Defects
Elasticity and anelasticity
Electrical properties
Equations of state
Fault zone rheology
Fracture and flow
Friction
High-pressure behaviour
Magnetic properties
Microstructure
Permeability and porosity
Phase transitions
Plasticity, diffusion, and creep

GENERAL SUBJECTS
Core
Gas and hydrate systems
Geomechanics
Geomorphology
Glaciology
Heat flow
Hydrogeophysics
Hydrology
Hydrothermal systems
Infrasound
Instrumental noise
Ionosphere/atmosphere interactions
Ionosphere/magnetosphere interactions
Mantle processes
Ocean drilling
Structure of the Earth
Thermochronology
Tsunamis
Ultra-high pressure metamorphism
Ultra-high temperature metamorphism

GEODESY and GRAVITY
Acoustic-gravity waves
Earth rotation variations
Geodetic instrumentation
Geopotential theory
Global change from geodesy
Gravity anomalies and Earth structure
Loading of the Earth
Lunar and planetary geodesy and gravity
Plate motions
Radar interferometry
Reference systems
Satellite geodesy
Satellite gravity
Sea level change
Seismic cycle
Space geodetic surveys
Tides and planetary waves
Time variable gravity
Transient deformation

GEOGRAPHIC LOCATION
Africa
Antarctica
Arctic region
Asia
Atlantic Ocean
Australia
Europe
Indian Ocean
Japan
New Zealand
North America
Pacific Ocean
South America

GEOMAGNETISM and ELECTROMAGNETISM
Archaeomagnetism
Biogenic magnetic minerals
Controlled source electromagnetics (CSEM)
Dynamo: theories and simulations
Electrical anisotropy
Electrical resistivity tomography (ERT)
Electromagnetic theory
Environmental magnetism
Geomagnetic excursions
Geomagnetic induction
Ground penetrating radar
Magnetic anomalies: modelling and interpretation
Magnetic fabrics and anisotropy
Magnetic field variations through time
Magnetic mineralogy and petrology
Magnetostratigraphy
Magnetotellurics
Marine electromagnetics
Marine magnetics and palaeomagnetics
Non-linear electromagnetics
Palaeointensity
Palaeomagnetic secular variation
Palaeomagnetism
Rapid time variations
Remagnetization
Reversals: process, time scale, magnetostratigraphy
Rock and mineral magnetism
Satellite magnetics

GEOPHYSICAL METHODS
Downhole methods
Fourier analysis
Fractals and multifractals
Image processing
Instability analysis
Interferometry
Inverse theory
Joint inversion
Neural networks, fuzzy logic
Non-linear differential equations
Numerical approximations and analysis
Numerical modelling
Numerical solutions
Persistence, memory, correlations, clustering
Probabilistic forecasting
Probability distributions
Self-organization
Spatial analysis
Statistical methods
Thermobarometry
Time-series analysis
Tomography
Waveform inversion
Wavelet transform

PLANETS
Planetary interiors
Planetary volcanism

SEISMOLOGY
Acoustic properties
Body waves
Coda waves
Computational seismology
Controlled source seismology
Crustal imaging
Earthquake dynamics
Earthquake early warning
Earthquake ground motions
Earthquake hazards
Earthquake interaction, forecasting, and prediction
Earthquake monitoring and test-ban treaty verification
Earthquake source observations
Guided waves
Induced seismicity
Interface waves
Palaeoseismology
Rheology and friction of fault zones
Rotational seismology
Seismic anisotropy
Seismic attenuation
Seismic instruments
Seismic interferometry
Seismicity and tectonics
Seismic noise
Seismic tomography
Site effects
Statistical seismology
Surface waves and free oscillations
Theoretical seismology

Tsunami warning
Volcano seismology
Wave propagation
Wave scattering and diffraction

TECTONOPHYSICS
Backarc basin processes
Continental margins: convergent
Continental margins: divergent
Continental margins: transform
Continental neotectonics
Continental tectonics: compressional
Continental tectonics: extensional
Continental tectonics: strike-slip and transform
Cratons
Crustal structure
Diapirism
Dynamics: convection currents, and mantle plumes
Dynamics: gravity and tectonics
Dynamics: seismotectonics
Dynamics and mechanics of faulting
Dynamics of lithosphere and mantle
Folds and folding
Fractures, faults, and high strain deformation zones
Heat generation and transport
Hotspots
Impact phenomena
Intra-plate processes
Kinematics of crustal and mantle deformation
Large igneous provinces
Lithospheric flexure
Mechanics, theory, and modelling
Microstructures
Mid-ocean ridge processes
Neotectonics
Obduction tectonics
Oceanic hotspots and intraplate volcanism
Oceanic plateaus and microcontinents
Oceanic transform and fracture zone processes
Paleoseismology
Planetary tectonics
Rheology: crust and lithosphere
Rheology: mantle
Rheology and friction of fault zones
Sedimentary basin processes
Subduction zone processes
Submarine landslides
Submarine tectonics and volcanism
Tectonics and climatic interactions
Tectonics and landscape evolution
Transform faults
Volcanic arc processes

VOLCANOLOGY
Atmospheric effects (volcano)
Calderas
Effusive volcanism
Eruption mechanisms and flow emplacement
Experimental volcanism
Explosive volcanism
Lava rheology and morphology
Magma chamber processes
Magma genesis and partial melting
Magma migration and fragmentation
Mud volcanism
Physics and chemistry of magma bodies
Physics of magma and magma bodies
Planetary volcanism
Pluton emplacement
Remote sensing of volcanoes
Subaqueous volcanism
Tephrochronology
Volcanic gases
Volcanic hazards and risks
Volcaniclastic deposits
Volcano/climate interactions
Volcano monitoring
Volcano seismology